Searching for the Cosmic Dawn

Thesis by

Michael William Eastwood

In Partial Fulfillment of the Requirements for the
Degree of
Doctor of Philosophy in Astrophysics

CALIFORNIA INSTITUTE OF TECHNOLOGY
Pasadena, California

2019
Defended September 3, 2018

Michael William Eastwood
ORCID: 0000-0002-4731-6083

ACKNOWLEDGEMENTS

[Add acknowledgements here. If you do not wish to add any to your thesis, you may simply add a blank titled Acknowledgements page.]

ABSTRACT

[This abstract must provide a succinct and informative condensation of your work. Candidates are welcome to prepare a lengthier abstract for inclusion in the dissertation, and provide a shorter one in the CaltechTHESIS record.]

PUBLISHED CONTENT AND CONTRIBUTIONS

[Fill this out with my publications]

TABLE OF CONTENTS

LIST OF ILLUSTRATIONS

LIST OF TABLES

Chapter 1

INTRODUCTION

1.1 Fundamental Physics

The discovery of the cosmic microwave background (CMB) radiation by Penzias & Wilson (1965) provided the first direct evidence that the universe had a beginning. Arno Penzias and Robert Wilson shared the 1978 Nobel Prize in Physics for this discovery, and astronomers have been studying this radiation ever since. In fact, a second Nobel Prize was awarded to John Mather and George Smoot in 2006 for their work on the Cosmic Background Explorer (COBE) satellite, which was amongst the first experiments to demonstrate that the background radiation was anisotropic (Smoot et al., 1992). These studies of the CMB have fundamentally advanced humanity's understanding of the universe: its origin, evolution, and composition. Still we continue to study the CMB particularly because it illuminates everything in the universe. It is a flashlight for the darkness of space within our expanding universe.

As the universe expands, the wavelength of a photon is similarly stretched or redshifted (so-called because it gradually drifts to longer, redder wavelengths). Photons originating from a star 1000 light-years away will travel through the universe for 1000 years before they are collected by our telescopes. Consequently, we observe this star as it was 1000 years ago. However, during its travels, the photon was also stretched by a small factor of 0.000007% due to the expansion of the universe. For nearby stars, this expansion factor is clearly too small to be conceivably measured. However, with the discovery of the first quasar by Schmidt (1963) it soon became apparent that the stretching factor, the redshift z, can be $> 10\%$. Today, the most distant known quasars and galaxies are so far away that the wavelength has more than doubled ($z > 1$) due to the expansion of the universe (Mortlock et al., 2011; Zitrin et al., 2015; Oesch et al., 2016; Bañados et al., 2018).

Due largely to careful and detailed work studying the CMB (e.g., Planck Collaboration et al., 2016), Type Ia supernova explosions (e.g., Riess et al., 1998; Perlmutter et al., 1999), and cosmological galaxy surveys (e.g., Colless et al., 2001), we have a coherent and consistent understanding of the expansion history of the universe. The redshift z is therefore commonly used as a proxy for distance. The higher the red-

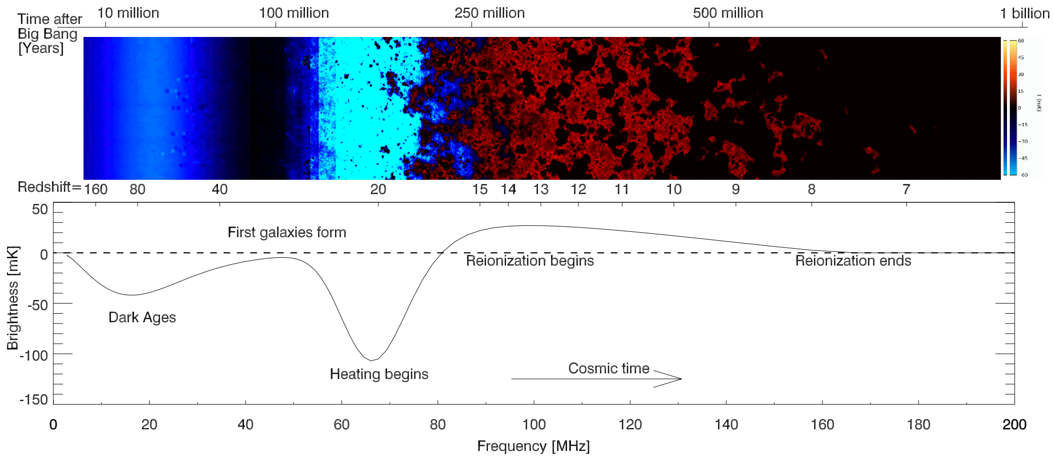

Figure 1.1: (top) A simulated light cone of the 21 cm brightness temperature illustrating the anisotropy in the expected signal. (bottom) A simulation of the globally averaged brightness temperature due to the high redshift 21 cm transition. This figure is reproduced with permission from Pritchard & Loeb (2012).

shift, the longer the photon has been in transit, and the further its origin. However, in order to measure the redshift, the measured photon must originate from a known spectral feature.

Despite its abundance, neutral hydrogen (H I) has few low energy transitions that allow it to be traced. Due to this limitation, astronomers resort to using a hyperfine structure transition arising from the magnetic dipole interaction between proton and electron. This interaction leads to a slight energy difference between the spin-symmetric state and the spin-antisymmetric state. The energy difference is $hc/(21\,\mathrm{cm})$ where h is Planck's constant, and c is the speed of light. When a Hydrogen atom transitions from the spin-symmetric state (higher energy) to the spin-antisymmetric state (lower energy), it emits a photon with a wavelength of 21 cm or a frequency of 1420 MHz. The redshift z of a 21 cm photon is therefore computed from the observed frequency ν as

$$z = \frac{1420\,\mathrm{MHz}}{\nu} - 1\,. \tag{1.1}$$

Neutral hydrogen in the early universe is illuminated by the CMB. A calculation of the radiative transfer (Pritchard & Loeb, 2012) yields (neglecting the contribution of peculiar velocities):

$$\Delta T_{21} \approx 27 \left[\overbrace{x_{\rm HI}(1+\delta)\left(\frac{\Omega_b h}{0.0327}\right)}^{\text{quantity of HI}} \left(\frac{\Omega_m}{0.307}\right)^{-1/2} \left(\frac{1+z}{10}\right)^{1/2} \overbrace{\left(\frac{T_{\rm spin} - T_{\rm CMB}(z)}{T_{\rm spin}}\right)}^{\text{relative temperature}} \right] \mathrm{m}K\,, \tag{1.2}$$

where ΔT_{21} is the expected 21 cm brightness temperature. If $\Delta T_{21} > 0$, it appears in emission against the CMB. If $\Delta T_{21} < 0$, it appears in absorption. $x_{\rm HI}$ is the neutral fraction of hydrogen, δ is the local baryon overdensity, h is the Hubble constant, Ω_b is the density parameter for baryons, Ω_m is the density parameter for matter, $T_{\rm spin}$ is the spin temperature (excitation temperature of the 21 cm transition), and $T_{\rm CMB}(z) = 2.73\,(1+z)\,\mathrm{K}$ is the temperature of the CMB at the redshift z.

Equation 1.2 is fundamental to determining what can be learned through detecting the 21 cm transition at high redshift. First, if the spin temperature is greater than the CMB temperature, the 21 cm transition appears in emission. However, the signal saturates at high spin temperatures. If the spin temperature is less than the CMB temperature, the 21 cm transition appears in absorption with no saturation point. Second, the amplitude of the signal is proportional to the total quantity of H I. Therefore, in order for there to be a measurable 21 cm signal, the universe must be predominantly neutral, and the transition must not be in radiative equilibrium with the CMB. An example prediction for ΔT_{21} can be seen in Figure 1.1.

There are three relevant temperatures that affect the spin temperature: $T_{\rm gas}$, the temperature of the gas, $T_{\rm CMB}$, the temperature of the CMB, and $T_{\rm Ly\alpha}$, the color temperature of the Lyα radiation from early star formation. More exotic theories might also include the temperature of the dark matter, $T_{\rm DM}$. Generally, the Lyα photons scatter through the intergalactic medium (IGM), which sets $T_{\rm Ly\alpha} = T_{\rm gas}$. In the absence of any heating mechanisms, the matter and radiation are both cooling adiabatically with the expansion of the universe. The adiabatic indices are $\gamma = 5/3$ and $\gamma = 4/3$ respectively, so the matter cools faster than the radiation. Consequently, the 21 cm transition tends to appear in absorption prior to early star formation, and in emission after the IGM has been heated.

While there are currently few observational constraints on the 21 cm brightness temperature, fiducial theoretical models tell the following story. During the dark ages ($z \gtrsim 40$) the density of the universe is high enough for collisions between hydrogen atoms to dominate the excitation of the 21 cm transition. Consequently

add a reference here

during this time $T_{\rm spin} = T_{\rm gas}$, and the 21 cm transition appears in absorption against the CMB. Later ($z \sim 30$), as the mean density of the universe decreases, collisions become more infrequent and the 21 cm transition is instead excited by CMB photons. During this time the 21 cm signal vanishes because $T_{\rm spin} = T_{\rm CMB}$.

With the onset of star formation in the universe, the IGM is inundated with Lyα photons. These Lyα photons scatter through the IGM. With the absorption and re-emission of a Lyα photon, a hydrogen atom can transition between the spin-symmetric state and the spin-antisymmetric state. This process, called the Wouthuysen-Field effect, sets the relative abundance of H I in each state such that $T_{\rm spin} = T_{\rm Ly\alpha} = T_{\rm gas}$ (Wouthuysen, 1952; Field, 1958). Therefore, after early star formation begins, the 21 cm transition reappears in absorption against the CMB.

However, as star formation progresses, the gas in the IGM is heated. X-rays are particularly effective at heating the IGM due to their large mean-free path. Consequently the heating rate is sensitive to, for example, the number density, luminosity and spectral hardness of X-ray binaries. Eventually the gas is heated above the temperature of the CMB, bringing the 21 cm transition into emission, and eventually the signal saturates. At this point the 21 cm transition begins to disappear with the onset of reionization at $z \lesssim 15$ due to the disappearance of neutral hydrogen. A prediction of the spectral distortion this process applies to the low-frequency ($\nu < 200\,$MHz) CMB spectrum can be seen in the bottom panel of Figure 1.1.

For much of the universe's history, the intergalactic medium (IGM) is ionized or in radiative equilibrium with the CMB.

Given knowledge of the original wavelength of the photon, and the expansion history of the universe, we can calculate how long the photon must have been in flight.

Today the CMB is a 2.7 K sea of photons that permeates the universe. This radiation is constantly cooling due to the inexorable expansion of the universe.

more context of other high-z probes of the universe

talk about Tzu-Ching's detection

1.2 First Generation Experiments

Ultimately, it may be possible to map the EoR and cosmic dawn through the 21 cm line (Madau et al., 1997). In fact, this is called a "main science goal" for the future Square Kilometer Array (SKA; Mellema et al., 2013). First generation experiments, however, are of somewhat more limited scope and therefore employ statistical averages to boost sensitivity to the high-redshift 21 cm signal.

The two most popular statistics are the global average and the power spectrum. The global average or monopole averages over all lines of sight, mapping the 21 cm brightness temperature within spherical shells of the universe:

$$T_{21}^{\text{global}}(z) = \frac{1}{\Omega} \int \Delta T_{21}(\vec{r})\, \mathrm{d}\Omega, \tag{1.3}$$

where $T_{21}^{\text{global}}(z)$ is the global 21 cm signal at the redshift z, $\Delta T_{21}(\vec{r})$ is the 21 cm brightness temperature at the position $\vec{r}$, and the integral runs over solid angle Ω. The power spectrum statistic leverages the line of sight distance information from the observed frequency to measure the power in fluctuations on a given spatial scale within a volume of the universe:

$$P_{21}(z; \vec{k}) = \frac{1}{V} \left| \int \Delta T_{21}(\vec{r})\, e^{-i\vec{k}\cdot\vec{r}}\, \mathrm{d}^3 r \right|^2, \tag{1.4}$$

where $P_{21}(z; \vec{k})$ is the three-dimensional spatial power spectrum at the redshift z and wavevector $\vec{k}$), and the integral runs over the observed volume V of the universe. Neglecting redshift-space distortions, the spatial power spectrum of 21 cm fluctuations is expected to be isotropic. Therefore, typically the power spectrum $P(\vec{k})$ is averaged over the orientation of the wavevector $\vec{k}$. Instrumental considerations typically lead to different sources of systematic errors along the line of sight and perpendicular to the line of sight, so parameterizing the power spectrum in terms of the parallel and perpendicular to the line of sight wavenumbers ($k_{\parallel}$ and $k_{\perp}$ respectively) is common.

The global signal and the power spectrum are both statistics of the same underlying 21 cm brightness temperature and therefore statistics can be used to answer high-level questions such as: When did reionization occur? How quickly was the universe heated after initial star formation began? The power spectrum contains additional information about sources of heating and ionization. For instance, rare massive haloes generate fluctuations on larger spatial scales than the more common small haloes. However, because measuring the power spectrum requires angular resolution, the global signal experiments and power spectrum experiments employ substantially different instrumental designs. They are subject to different (but not exclusively different) systematic instrumental errors.

Global Signal Experiments

Most global signal experiments are composed of a single dipole antenna with a total power radiometer. This approach was pioneered by the Experiment to Detect the Global EoR Signature (EDGES). After deploying to the Murchison Radio-astronomy Observatory (MRO) in a remote region of Western Australia, Bowman & Rogers (2010) observed for three months. If reionization was an instantaneous event, this initial EDGES deployment would have expected to see a step function in their sky-averaged spectrum. Therefore the authors converted the observed spectral smoothness to a lower bound on the duration of reionization $\Delta z > 0.06$. However, because no such feature was detected, the redshift of reionization was not constrained by this measurement.

LEDA

SARAS

Although most global signal experiments are composed of isolated dipole antennas, there have been several attempts to design and use more exotic instruments. Liu et al. (2013) found that an instrument with a 5° beam could achieve a higher significance detection by using the improved angular resolution to mitigate foreground contamination. Vedantham et al. (2015) used lunar occultation to constrain the global signal between 35 and 80 MHz using LOFAR. This technique uses an interferometer to measure the contrast between the moon and surrounding sky, but is complicated by radio frequency interference (RFI) reflecting off of the moon and potentially by the assumption that the moon is a thermal source at low frequencies. Drawn by the calibration advantages of interferometers, other groups have proposed designing interferometers that have nonzero sensitivity to the monopole. Presley et al. (2015) developed a framework for measuring the global signal from interferometric measurements, and Singh et al. (2015) designed a zero-spacing interferometer using a resistive screen to separate two antennas. However, ultimately the calibration advantages of an interferometer to measure the global signal may have been overstated. Venumadhav et al. (2016) demonstrated that interferometers may only have any sensitivity to the global signal if there is some amount of cross talk between the correlated elements or a source of noise that can radiate coherently into both receivers.

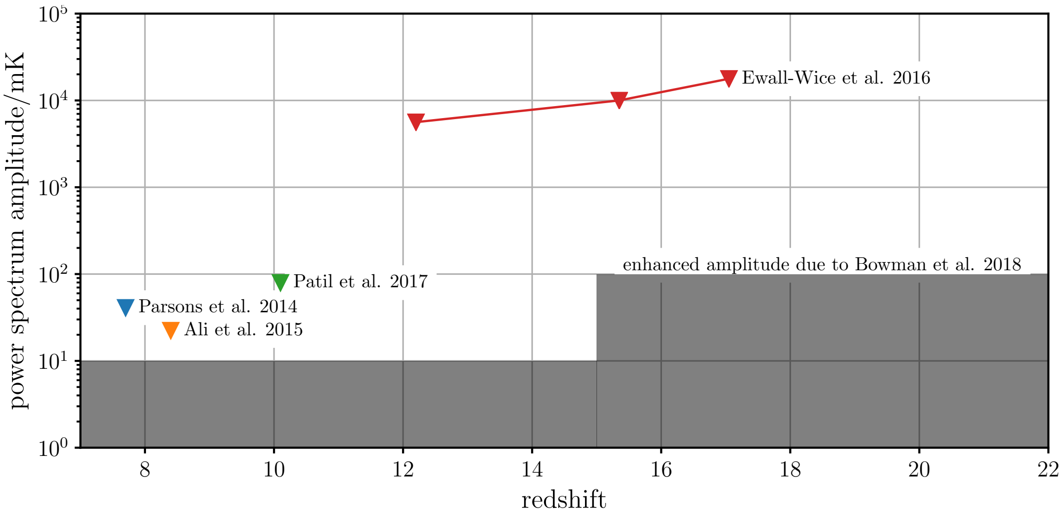

Figure 1.2: Power spectrum amplitude upper limits (95% confidence) as a function of redshift. The shaded region denotes roughly where current theoretical predictions fall.

Power Spectrum Experiments

In contrast to the global signal experiments, which are typically composed of a single antenna, power spectrum experiments are generally interferometers composed of up to hundreds or thousands of antennas. A high-level overview of existing upper limits on the 21 cm power spectrum can be seen in Figure 1.2.

The Donald C. Backer Precision Array for Probing the Epoch of Reionization (PAPER; Parsons et al., 2010) began attempting to measure the 21 cm power spectrum with a deployment of eight antennas in Green Bank, West Virginia. Later deployed with 32 antennas to the Karoo desert in South Africa, Parsons et al. (2014) measured a 2σ upper limit of 41 mK on the amplitude of the power spectrum at $z = 7.7$. This measurement ruled out the possibility that the universe was entirely unheated by this redshift. Later, with PAPER now composed of 64 antennas, Ali et al. (2015) improved the best 2σ upper limit to 22.4 mK at $z = 8.4$, however this is result is currently subject to revision (Cheng et al. in prep.). PAPER is notable for its decision to part with traditional interferometry. Starting with its 32-antenna deployment, PAPER opted for a maximally redundant antenna configuration for raw sensitivity on a particular spatial scale.

The Low-Frequency Array (LOFAR) EoR Key Science Project (KSP) is attempting a similar measurement of the 21 cm power spectrum. In contrast to PAPER, LOFAR is composed of $\sim 30,000$ high-band antennas (120–240 MHz) and $\sim 3,000$ lowband antennas (30–80 MHz). These antennas are grouped into stations and stations are correlated with each other. This trade off sacrifices field of view for gain. The LOFAR EoR KSP recently published its first limits on the 21 cm power spectrum, finding a 2σ upper limit of 79.6 mK at $z = 10.1$ (Patil et al., 2017). In this measurement, LOFAR attempted to leverage its superior imaging and source-removal capabilities, but for this measurement was limited by residual systematic errors. The removal of contaminating diffuse radio emission has been the focus of ongoing work with some reported success (Koopmans, 2017).

Several attempts have been made to measure the 21 cm power spectrum with the Murchison Widefield Array (MWA). MWA

1.3 Observational Challenges

Likely the most substantial challenge faced by both classes of experiments is the existence of foreground radio emission. At large angular scales $\theta \gg 1^\circ$, the radio sky is dominated by galactic synchrotron emission generated by relativistic electrons spiralling around galactic magnetic field lines. The EDGES experiment, in the southern hemisphere, measured the brightness temperature of this emission to be (Mozdzen et al., 2017)

$$T \sim 300\,\mathrm{K} \times \left(\frac{\nu}{150\,\mathrm{M}Hz}\right)^{-2.6}. \tag{1.5}$$

At smaller angular scales $\theta \lesssim 1^\circ$, the galactic emission gives way to a sea of active galactic nuclei (AGN), the brightest of which, Cyg A, has a flux $> 15,000$ Jy at frequencies < 80 MHz (Baars et al., 1977). A simple comparison between Equations 1.2 and 1.5 reveals that the foreground radio emission must be suppressed by four to five orders of magnitude. However, this foreground emission is typically synchrotron and free-free, which are both spectrally smooth. The 21 cm signal, on the other hand, is not expected to be so smooth. This is due to the fact that sweeping through frequency along a line of sight probes different causally disconnected regions of the universe. Each of these regions experiences a different star formation, heating and reionization history, which ultimately produces a different 21 cm brightness temperature. However, at the same time there is a relative paucity of suitable modern, high-fidelity sky maps at these frequencies.

Global-signal experiments have no intrinsic angular resolution of their own. To date, these experiments have typically relied on low-order polynomial fits to remove the foreground contamination in their measurements. This is a fine balancing

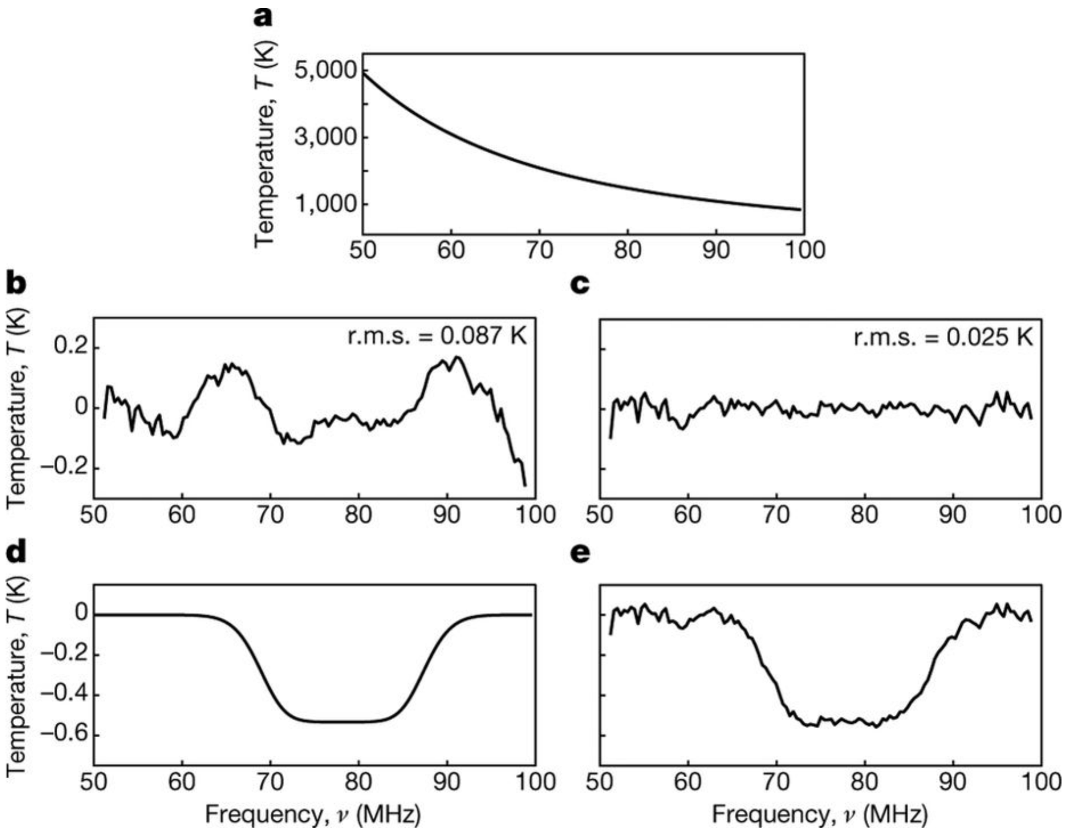

Figure 1.3: (a) The calibrated sky spectrum measured by the EDGES experiment. (b) The residuals after fitting a model of the foreground emission. (c) The residuals after performing a joint fit of the foreground emission and an absorption trough. (d) The best-fit absorption trough. (e) The best-fit absorption trough including residual noise. This figure is reproduced with permission from Bowman et al. (2018).

routine, because if the polynomial order is chosen to be too low, residual foreground contamination dominates the measurement. If the polynomial order is chosen to be too high, the 21 cm signal itself can be removed.

1.4 Future Outlook

Recently, a significant development came from the first putative detection of the global 21 cm signal by the EDGES experiment (Bowman et al., 2018). In this paper, the authors claimed a detection of an absorption feature centered at 78 MHz, which they attribute to early star formation and heating (see Figure 1.3). If true, this detection is remarkable for its extreme $\sim$ 500 mK amplitude. In order to generate such a large absorption feature, either the IGM needs to be cooled below temperatures it is possible to reach purely through adiabatic cooling, or an additional source of radio emission must be present at $z > 20$.

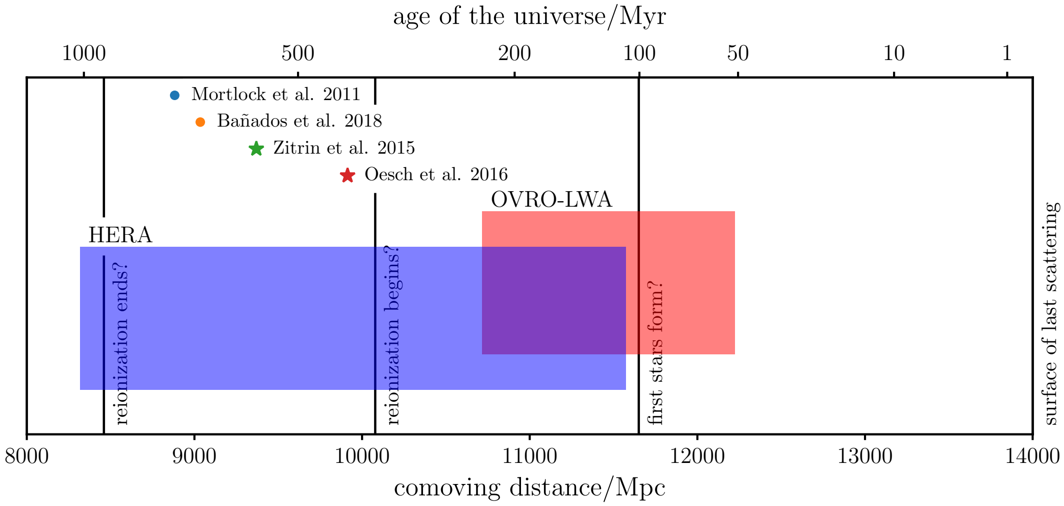

Figure 1.4: A radial map of the universe. Known quasars are marked with circles and galaxies are marked with stars. The range of comoving distances probed by the OVRO-LWA and HERA are marked with a red rectangle and a blue rectangle respectively.

Bibliography

Ali, Z. S., Parsons, A. R., Zheng, H., et al. 2015, ApJ, 809, 61

Baars, J. W. M., Genzel, R., Pauliny-Toth, I. I. K., & Witzel, A. 1977, A&A, 61, 99

Bañados, E., Venemans, B. P., Mazzucchelli, C., et al. 2018, Nature, 553, 473

Bowman, J. D., & Rogers, A. E. E. 2010, Nature, 468, 796

Bowman, J. D., Rogers, A. E. E., Monsalve, R. A., Mozdzen, T. J., & Mahesh, N. 2018, Nature, 555, 67

Colless, M., Dalton, G., Maddox, S., et al. 2001, MNRAS, 328, 1039

Field, G. B. 1958, Proceedings of the IRE, 46, 240

Koopmans, L. V. E. 2017, Proceedings of the International Astronomical Union, 12, 71–76

Liu, A., Pritchard, J. R., Tegmark, M., & Loeb, A. 2013, Phys. Rev. D, 87, 043002

Madau, P., Meiksin, A., & Rees, M. J. 1997, ApJ, 475, 429

Mellema, G., Koopmans, L. V. E., Abdalla, F. A., et al. 2013, Experimental Astronomy, 36, 235

Mortlock, D. J., Warren, S. J., Venemans, B. P., et al. 2011, Nature, 474, 616

Mozdzen, T. J., Bowman, J. D., Monsalve, R. A., & Rogers, A. E. E. 2017, MNRAS, 464, 4995

Oesch, P. A., Brammer, G., van Dokkum, P. G., et al. 2016, ApJ, 819, 129

Parsons, A. R., Backer, D. C., Foster, G. S., et al. 2010, AJ, 139, 1468

Parsons, A. R., Liu, A., Aguirre, J. E., et al. 2014, ApJ, 788, 106

Patil, A. H., Yatawatta, S., Koopmans, L. V. E., et al. 2017, ApJ, 838, 65

Penzias, A. A., & Wilson, R. W. 1965, ApJ, 142, 419

Perlmutter, S., Aldering, G., Goldhaber, G., et al. 1999, ApJ, 517, 565

Planck Collaboration, Ade, P. A. R., Aghanim, N., et al. 2016, A&A, 594, A25

Presley, M. E., Liu, A., & Parsons, A. R. 2015, ApJ, 809, 18

Pritchard, J. R., & Loeb, A. 2012, Reports on Progress in Physics, 75, 086901

Riess, A. G., Filippenko, A. V., Challis, P., et al. 1998, AJ, 116, 1009

Schmidt, M. 1963, Nature, 197, 1040

Singh, S., Subrahmanyan, R., Udaya Shankar, N., & Raghunathan, A. 2015, ApJ, 815, 88

Smoot, G. F., Bennett, C. L., Kogut, A., et al. 1992, ApJ, 396, L1

Vedantham, H. K., Koopmans, L. V. E., de Bruyn, A. G., et al. 2015, MNRAS, 450, 2291

Venumadhav, T., Chang, T.-C., Doré, O., & Hirata, C. M. 2016, ApJ, 826, 116

Wouthuysen, S. A. 1952, AJ, 57, 31

Zitrin, A., Labbé, I., Belli, S., et al. 2015, ApJ, 810, L12

Chapter 2

A PATH TOWARDS CALIBRATION OF THE OVRO-LWA

2.1 Design and Construction of the OVRO-LWA

The Owens Valley Radio Observatory Long Wavelength Array (OVRO-LWA) is a new low-frequency radio interferometer constructed during the course of this thesis (see Figure 2.1). In its current iteration, it is composed of 288 dual-polarization dipole antennas with a bandpass covering 27 to 85 MHz (wavelengths between 3.5 and 11 m). 251 antennas are located with a 200 m diameter core in a pseudo-random configuration optimized for minimum sidelobes in snapshot imaging. 32 additional antennas are located at distances up to 1.5 km from the core of the array. At 85 MHz, the OVRO-LWA can therefore achieve an angular resolution of $8'$. Figures 2.2 and 2.3 illustrate the improvement in angular resolution associated with using these long baselines.

The OVRO-LWA hosts the LEDA correlator (Kocz et al., 2015), which performs full cross-correlation of 512 input signals.

Paragraph on antenna

Paragraph on receivers

Paragraph on correlator

During observations, data is streamed from the LEDA correlator to the All-Sky Transient Monitor (ASTM), which houses the compute nodes used for post-processing, imaging, and the analysis completed in this thesis.

ASTM is composed of 10 identical nodes.

Fill out specs once ASTM is back online....

There are two complementary software pipelines that service the scientific goals of the OVRO-LWA:

1. A widefield snapshot imaging pipeline that images the entire visible hemisphere every 13 s.
2. A novel approach specialized for drift-scanning interferometers that can image the entire sky (above a limiting declination) in a single synthesis imaging step.

The latter pipeline will be discussed in considerable depth in Chapters 3 and 4.

(a) (b)

Figure 2.1: (a) A picture of an OVRO-LWA antenna. (b) A view of the OVRO-LWA with the Sierra Mountains in the background.

2.2 Calibration of a Low-Frequency Interferometer

Gain calibration amounts to determining the optimal set of Jones matrices G_i for each antenna i such that

$$\boldsymbol{V}_{ij,\text{measured}} = \boldsymbol{G}_i \boldsymbol{V}_{ij,\text{model}} \boldsymbol{G}_j^* + \boldsymbol{N}_{ij} \tag{2.1}$$

$$\begin{pmatrix} V_{ij,\text{measured}}^{xx} & V_{ij,\text{measured}}^{xy} \\ V_{ij,\text{measured}}^{yx} & V_{ij,\text{measured}}^{yy} \end{pmatrix} = \begin{pmatrix} g_i^{xx} & g_i^{xy} \\ g_i^{yx} & g_i^{yy} \end{pmatrix} \begin{pmatrix} V_{ij,\text{model}}^{xx} & V_{ij,\text{model}}^{xy} \\ V_{ij,\text{model}}^{yx} & V_{ij,\text{model}}^{yy} \end{pmatrix} \begin{pmatrix} g_j^{xx} & g_j^{xy} \\ g_j^{yx} & g_j^{yy} \end{pmatrix}^* + \begin{pmatrix} n_j^{xx} & n_j^{xy} \\ n_j^{yx} & n_j^{yy} \end{pmatrix}, \tag{2.2}$$

where $\boldsymbol{V}_{ij,\text{measured}}$ is the Jones matrix of measured visibilities on the baseline $i-j$, $\boldsymbol{V}_{ij,\text{model}}$ is the Jones matrix of model visibilities (i.e., ideally what would have been measured if the antenna and receiver did not impart any additional gain or phase), and $\boldsymbol{N}_{ij}$ is additional noise.

A typical calibration strategy using the Very Large Array (VLA) involves periodically pointing at a known compact point source. For a compact point source at the phase center, the phase of all visibilities should be zero, and the amplitude is given by the known flux (and if necessary, the polarization) of the source.

The OVRO-LWA is capable of imaging the entire hemisphere in a snapshot image. This brings its own unique calibration challenges because it is currently impossible to isolate a single compact point source within the field of view of the interferometer.[1] Due to the wide field of view, determining an accurate gain calibration relies on a detailed sky and antenna beam model. Mistakes or omissions in the sky model can, for example, generate artificial ripples in the bandpass calibration that will

[1] Gated pulsar observations could, in principle, achieve this isolation. This capability is a key development area for the OVRO-LWA.

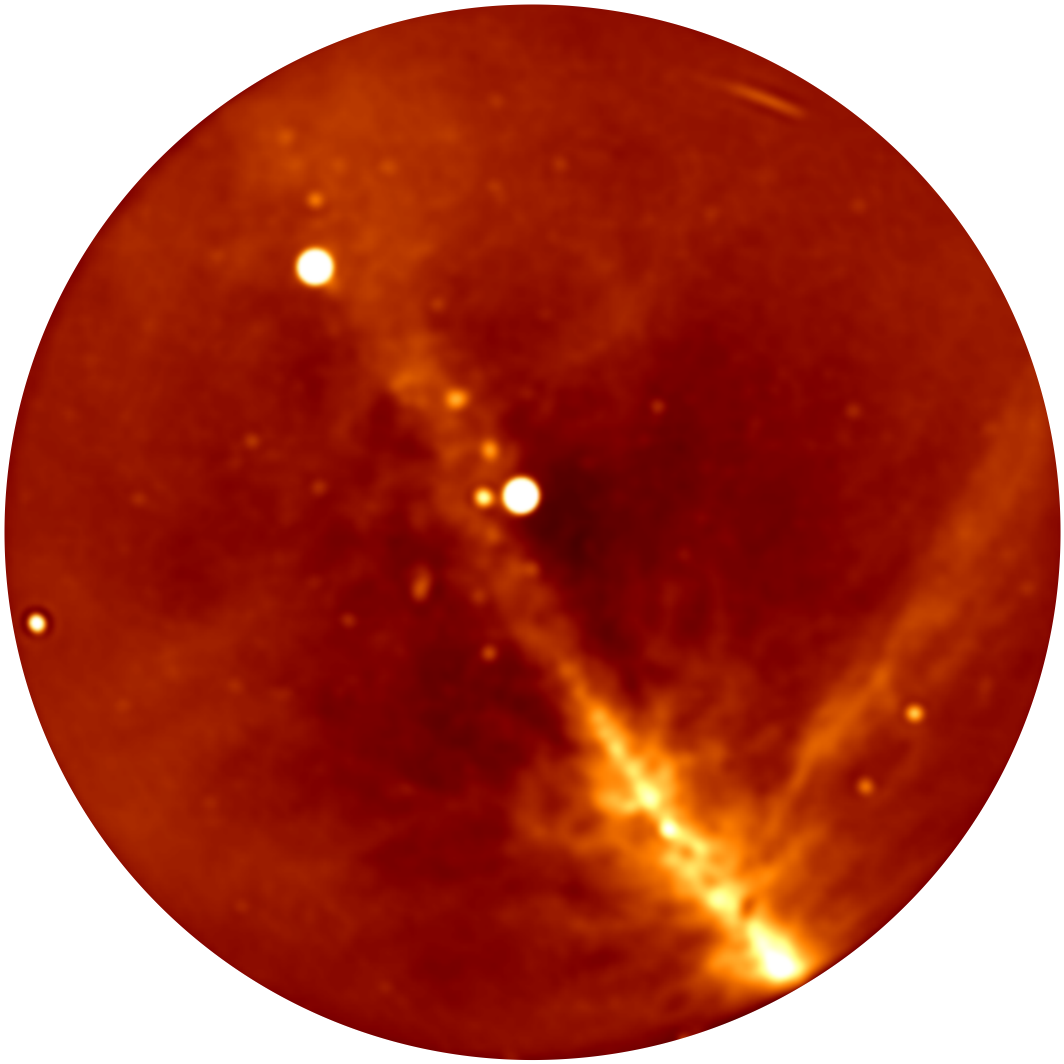

Figure 2.2: Snapshot dirty image of the sky captured with the OVRO-LWA using just the antennas located in the core of the array. Cyg A and Cas A have been peeled and restored with model sources.

impact the interferometer's ability to cleanly separate foreground emission from cosmological 21 cm emission (Barry et al., 2016).

Furthermore, at frequencies $\nu < 100$ MHz there are few flux calibrators. Baars et al. (1977) determined the absolute spectrum of Cyg A between 20 MHz and 2 GHz. Scaife & Heald (2012) added six additional calibrators, and Perley & Butler (2017) used the VLA 4-band system to bring the total number of available calibrators to 11. However, in §3.3 I will show that the latter spectra can diverge rapidly from truth below 50 MHz.

Detailed sky and beam models are therefore generally an important calibration

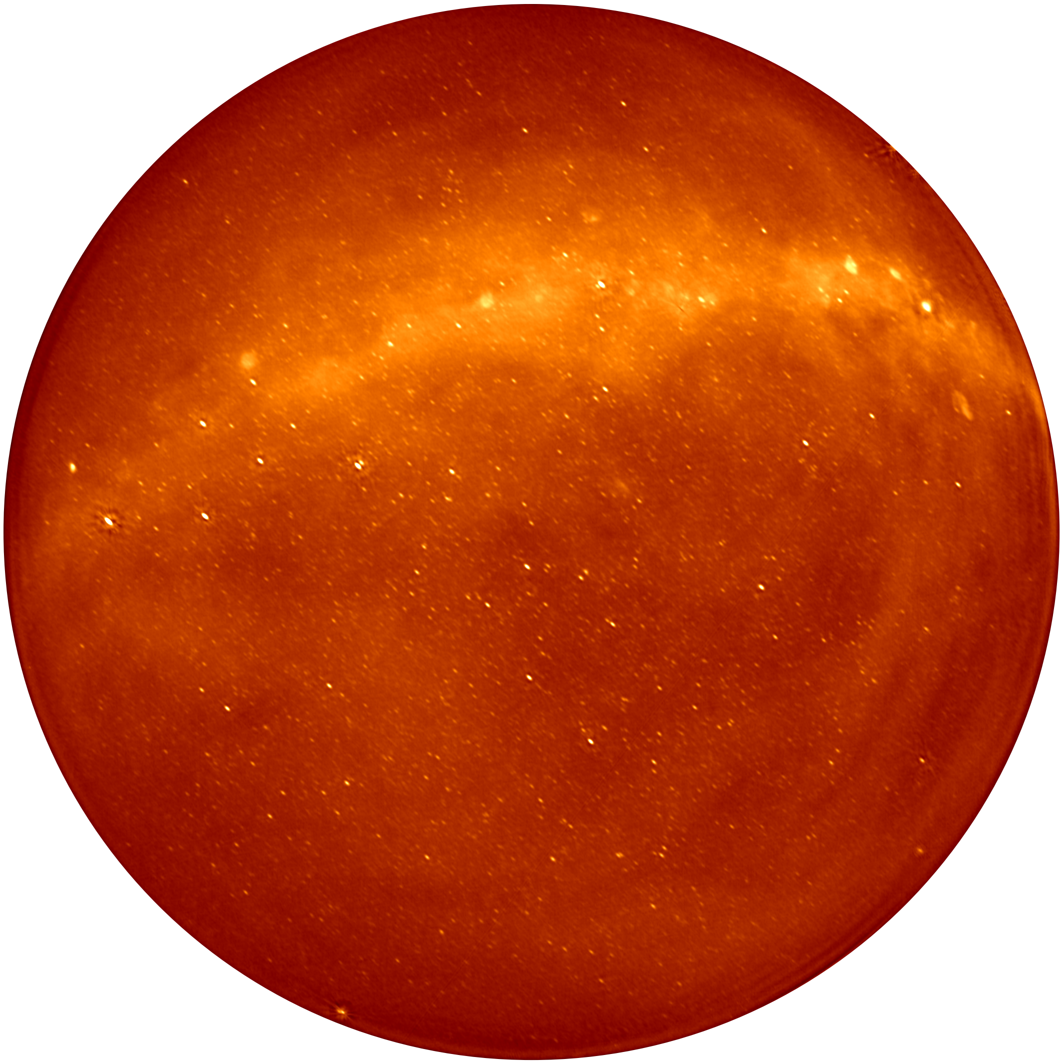

Figure 2.3: Snapshot image of the sky captured with the OVRO-LWA using the new long-baseline antennas.

requirement for low-frequency interferometers. In §3, I derived an empirical beam model for the OVRO-LWA and developed a new imaging formalism that captures the entire visible sky in a single synthesis imaging step that can be used as part of a self-calibration loop.

The calibration routine itself is adapted from a variant of alternating least-squares developed by Mitchell et al. (2008) and Salvini & Wijnholds (2014). At each step this algorithm seeks to minimize

$$\boldsymbol{G}_i = \operatorname{argmin} \sum_{j \neq i} \left\| \boldsymbol{V}_{ij,\text{measured}} - \boldsymbol{G}_i \boldsymbol{V}_{ij,\text{model}} \boldsymbol{G}_j^* \right\|^2 \tag{2.3}$$

where each of the elements of $\boldsymbol{G}_j^*$ are considered fixed. Equation 2.3 is therefore a linear least-squares optimization and can be rapidly solved. However, by fixing $\boldsymbol{G}_j^*$ these iterations tend to oscillate about a minimum of χ^2. These oscillations can be damped by averaging subsequent iterations, and Salvini & Wijnholds (2014) demonstrated that this simple gradient-free optimization strategy converges remarkably quickly.

Some interferometers (e.g., HERA and the MWA), recognizing the difficulty of gain calibration at low frequencies, have opted for partly redundant antenna configurations. These configurations can solve for many of their calibration parameters internally without relying on an incomplete sky model and potentially inaccurate antenna beam model (Liu et al., 2010). However, these interferometers sacrifice imaging fidelity, which is useful for establishing the remaining calibration parameters (e.g., the overall bandpass cannot be solved for in an internal redundant-calibration routine).[2]

2.3 Source Removal and Direction-Dependent Calibration

Because the OVRO-LWA antenna layout is optimized for sidelobe levels in snapshot imaging, the point-spread function (PSF) is pretty good.

Bibliography

Baars, J. W. M., Genzel, R., Pauliny-Toth, I. I. K., & Witzel, A. 1977, A&A, 61, 99

Barry, N., Hazelton, B., Sullivan, I., Morales, M. F., & Pober, J. C. 2016, MNRAS, 461, 3135

Kocz, J., Greenhill, L. J., Barsdell, B. R., et al. 2015, Journal of Astronomical Instrumentation, 4, 1550003

Liu, A., Tegmark, M., Morrison, S., Lutomirski, A., & Zaldarriaga, M. 2010, MNRAS, 408, 1029

Mitchell, D. A., Greenhill, L. J., Wayth, R. B., et al. 2008, IEEE Journal of Selected Topics in Signal Processing, 2, 707

Perley, R. A., & Butler, B. J. 2017, ApJS, 230, 7

Salvini, S., & Wijnholds, S. J. 2014, A&A, 571, A97

Scaife, A. M. M., & Heald, G. H. 2012, MNRAS, 423, L30

[2] The HERA collaboration is currently investigating the possibility of determining the overall bandpass through redundancies between frequency channels. The author of this thesis is not optimistic about this approach.

Chapter 3

THE RADIO SKY AT METER WAVELENGTHS: M-MODE ANALYSIS IMAGING WITH THE OVRO-LWA

Eastwood, M. W., Anderson, M. M., Monroe, R. M., et al. 2018, The Astronomical Journal, 156, 32. http://stacks.iop.org/1538-3881/156/i=1/a=32

Abstract

A host of new low-frequency radio telescopes seek to measure the 21 cm transition of neutral hydrogen from the early universe. These telescopes have the potential to directly probe star and galaxy formation at redshifts $20 \gtrsim z \gtrsim 7$, but are limited by the dynamic range they can achieve against foreground sources of low-frequency radio emission. Consequently, there is a growing demand for modern, high-fidelity maps of the sky at frequencies below 200 MHz for use in foreground modeling and removal. We describe a new wide-field imaging technique for drift-scanning interferometers: Tikhonov-regularized m-mode analysis imaging. This technique constructs images of the entire sky in a single synthesis imaging step with exact treatment of wide-field effects. We describe how the CLEAN algorithm can be adapted to deconvolve maps generated by m-mode analysis imaging. We demonstrate Tikhonov-regularized m-mode analysis imaging using the Owens Valley Radio Observatory Long Wavelength Array (OVRO-LWA) by generating eight new maps of the sky north of $\delta = -30°$ with $15'$angular resolution at frequencies evenly spaced between 36.528 and 73.152 MHz, and ~800 mJy/beam thermal noise. These maps are a 10-fold improvement in angular resolution over existing full-sky maps at comparable frequencies, which have angular resolutions $\geq 2°$. Each map is constructed exclusively from interferometric observations and does not represent the globally averaged sky brightness. Future improvements will incorporate total power radiometry, improved thermal noise, and improved angular resolution due to the planned expansion of the OVRO-LWA to 2.6 km baselines. These maps serve as a first step on the path to the use of more sophisticated foreground filters in 21 cm cosmology incorporating the measured angular and frequency structure of all foreground contaminants.

3.1 Introduction

At redshifts $20 \gtrsim z \gtrsim 7$, the 21 cm hyperfine structure line of neutral hydrogen is expected to produce a 10 to 100 mK perturbation in the cosmic microwave background (CMB) spectrum (Furlanetto et al., 2006; Pritchard & Loeb, 2012). The amplitude of this perturbation on a given line of sight is a function of the neutral fraction of hydrogen, the baryon overdensity, the spin temperature relative to the CMB temperature at the given redshift, and the line-of-sight peculiar velocity of the gas. The spatial power spectrum of this perturbation is thought to be dominated by inhomogeneous heating of the intergalactic medium (IGM) at $z \sim 20$ (Fialkov et al., 2014), and by growing ionized bubbles during the epoch of reionization (EoR) at $z \sim 7$, where a detection can constrain the ionizing efficiency of early galaxies, the UV photon mean-free path, and the minimum halo mass that can support star formation (Greig & Mesinger, 2015).

Current 21 cm cosmology experiments can be broadly separated into two classes: global signal experiments that aim to detect the spectral signature of the cosmologically redshifted 21 cm transition after averaging over the entire sky (otherwise known as the monopole) and power spectrum experiments that incorporate angular information to attempt to measure the 3D spatial power spectrum of cosmological 21 cm perturbations. Ongoing global signal experiments include EDGES (Monsalve et al., 2017), LEDA (Price et al., 2017), BIGHORNS (Sokolowski et al., 2015), SCI-HI (Voytek et al., 2014), and SARAS 2 (Singh et al., 2017). Ongoing power spectrum experiments include PAPER/HERA (Ali et al., 2015; DeBoer et al., 2016), LOFAR (Patil et al., 2017), and the MWA (Beardsley et al., 2016; Ewall-Wice et al., 2016). Recently, EDGES reported the first detection of 21 cm absorption in the globally averaged sky signal (Bowman et al., 2018).

Just as for CMB experiments, foreground removal or suppression is an essential component of both classes of 21 cm cosmology experiments. The brightness temperature of the galactic synchrotron emission at high galactic latitudes is measured by Mozdzen et al. (2017) as

$$T \sim 300\,\mathrm{K} \times \left(\frac{\nu}{150\,\mathrm{M}Hz}\right)^{-2.6}. \tag{3.1}$$

Therefore, experiments conservatively need to achieve five orders of dynamic range against this foreground emission before the cosmological signal can be measured. Current foreground removal methods (for example, Parsons et al. 2012 and Chapman et al. 2013) rely on the assumption that the foreground emission is spectrally smooth. The low-frequency radio sky is composed of several components: galactic synchrotron emission, supernova remnants, radio galaxies, free-free emission and absorption from H II regions, and a confusing background of radio sources. Ideally, a foreground removal strategy should be informed by the measured spatial structure and frequency spectrum of all foreground components. For instance, CMB experiments typically construct several maps at several frequencies to enable component separation. At low frequencies, this possibility is limited by the availability of suitable high-fidelity sky maps on angular scales ranging from tens of degrees to arcminutes.

Recently, a host of new low-frequency sky surveys have been conducted, including MSSS (Heald et al., 2015), GLEAM (Wayth et al., 2015), and TGSS (Intema et al., 2017). However, the primary data product generated by these surveys is a catalog of radio point sources. At 45 MHz, Guzmán et al. (2011) created a map of the sky that captures the diffuse emission with 5° resolution. The LWA1 Low Frequency Sky Survey (LLFSS; Dowell et al., 2017) similarly maps the sky at a range of frequencies between 35 and 80 MHz with resolution between 4.5° and 2°.

The Global Sky Model (GSM; de Oliveira-Costa et al., 2008) is currently the most commonly used foreground model. The GSM is a nonparametric interpolation of various maps between 10 MHz and 100 GHz. However, the majority of information contained in the GSM is derived at frequencies > 1.4 GHz, where the majority of the modern, high-fidelity input maps are located. At 408 MHz, the venerable Haslam map (Haslam et al., 1981, 1982) covers the entire sky at 1° resolution. Below 408 MHz, the GSM uses three input sky maps. Zheng et al. (2017a) constructed an improved GSM with five maps below 408 MHz, and Dowell et al. (2017) used the LWA1 to improve the GSM with their own sky maps. However, the GSM generally suffers from low angular resolution ($\sim 5^\circ$) and systematic errors associated with instrumental artifacts in the input maps. For instance, Dowell et al. (2017) reported errors of $\pm 50\%$ between the GSM and their own maps at 74 MHz, which they attribute to the increasing contribution of free-free absorption and modifications to the synchrotron spectral index at low frequencies.

Wide-field interferometric synthesis imaging is a challenging computational problem, and it has been particularly difficult to capture large angular scales $\gg 10^\circ$ and small angular scales $\ll 1^\circ$ in a single synthesis image. We will derive a new imaging technique – Tikhonov-regularized m-mode analysis imaging – that allows a drift-scanning interferometer to image the entire visible sky in a single coherent synthesis imaging step with no gridding and no mosaicking.

As a demonstration of this technique, we apply Tikhonov-regularized m-mode analysis imaging to the Owens Valley Radio Observatory Long Wavelength Array (OVRO-LWA) and generate a series of new low-frequency maps of the sky between 36.528 and 73.152 MHz. These maps capture the full sky visible from OVRO with an angular resolution of ~ 15 arcmin. These new maps complement the existing full-sky maps at these frequencies with greatly improved angular resolution.

We aim for these maps to inform foreground removal strategies in 21 cm cosmology, and we anticipate additional ancillary science taking advantage of the combination of high fidelity and high resolution of these maps, including but not limited to studies of the cosmic-ray emissivity at low frequencies, searches for giant radio galaxies, and constraining the galactic synchrotron spectrum. The maps will be made freely available online at the Legacy Archive for Microwave Background Data Analysis (LAMBDA)[1].

The structure of this paper is as follows. In §3.2, we present Tikhonov-regularized m-mode analysis imaging, a new imaging technique that allows us to image the entire visible sky in one coherent synthesis imaging step with exact wide-field corrections. In §3.3 we describe our observations with the OVRO-LWA. In §3.4 we present the sky maps and compare these maps against other low-frequency sky maps. In §3.5, we discuss some of the sources of error present in the maps, and finally, in §3.6 we present our conclusions.

3.2 All-sky Imaging

The goal of all imaging algorithms is to estimate the brightness of the sky $I_\nu(\hat{r})$ in the direction $\hat{r}$ and frequency ν. A radio interferometer measures the visibilities $V_\nu^{ij,pq}$ between pairs of antennas numbered i and j respectively, and between polarizations labeled p and q respectively. We will neglect subtleties associated with polarized imaging, so the Stokes I visibilities are constructed from the sum of the pp and qq correlations such that $V_\nu^{ij} = (V_\nu^{ij,pp} + V_\nu^{ij,qq})/2$. If the antennas are separated by the baseline $\vec{b}_{ij}$, and $A_\nu(\hat{r})$ describes an antenna's response to the incident Stokes I radiation (here assumed to be the same for each antenna), then

$$V_\nu^{ij} = \int_{\text{sky}} A_\nu(\hat{r}) I_\nu(\hat{r}) \exp\left(2\pi i \hat{r}\cdot \vec{b}_{ij}/\lambda\right) \mathrm{d}\Omega, \tag{3.2}$$

[1] `https://lambda.gsfc.nasa.gov/product/foreground/fg_ovrolwa_radio_maps_info.cfm`

where the integral runs over the solid angle Ω. Constructing an image from the output of a radio interferometer consists of estimating $I_\nu(\hat{r})$ given the available measurements V_ν^{ij}.

For later convenience, we will define the baseline transfer function $B_\nu^{ij}(\hat{r})$ such that

$$V_\nu^{ij} = \int_{\text{sky}} B_\nu^{ij}(\hat{r}) I_\nu(\hat{r})\,\mathrm{d}\Omega\,. \tag{3.3}$$

The baseline transfer function defines the response of a single baseline to the sky and is a function of the antenna primary beam, and baseline length and orientation.

Naively, one might attempt to solve Equation 3.2 by discretizing and subsequently solving the resulting matrix equation. If the interferometer is composed of N_{base} baselines and measures N_{freq} frequency channels over N_{time} integrations, then the entire data set consists of $N_{\text{base}}N_{\text{freq}}N_{\text{time}}$ complex numbers. If the sky is discretized into N_{pix} pixels, then the relevant matrix has dimensions of $(N_{\text{base}}N_{\text{freq}}N_{\text{time}})\times(N_{\text{pix}})$. For making single-channel maps with the OVRO-LWA, this becomes a 5 PB array (assuming each matrix element is a 64 bit complex floating point number). This matrix equation is therefore prohibitively large, and solving Equation 3.2 by means of discretization is usually intractable, although Zheng et al. (2017b) demonstrated this technique with the MITEOR telescope.

Instead, it is common to make mild assumptions that simplify Equation 3.2 and ease the computational burden in solving for $I_\nu(\hat{r})$. For example, when all of the baselines $\vec{b}_{ij}$ lie in a plane and the field of view is small, Equation 3.2 can be well approximated by a two-dimensional Fourier transform (Thompson et al., 2001). The restriction on baseline coplanarity and field of view can be relaxed by using W-projection (Cornwell et al., 2008). Known primary beam effects can also be accounted for during imaging by using A-projection (Bhatnagar et al., 2013).

m-mode Analysis

Transit telescopes can take advantage of a symmetry in Equation 3.2 that greatly reduces the amount of computer time required to image the full sky with exact incorporation of wide-field imaging effects. This technique, called m-mode analysis, also obviates the need for gridding and mosaicking. Instead, the entire sky is imaged in one coherent synthesis imaging step. We will briefly summarize m-mode analysis below, but the interested reader should consult Shaw et al. (2014, 2015) for a complete derivation.

In the context of m-mode analysis, a transit telescope is any interferometer for which the response pattern of the individual elements does not change with respect to time. This may be an interferometer like the OVRO-LWA, where the correlation elements are fixed dipoles, but it may also be an interferometer like LOFAR or the MWA if the steerable beams are held in a fixed position (not necessarily at zenith). The interferometer also does not necessarily have to be homogeneous. Heterogeneous arrays composed of several different types of antennas are allowed as long as care is taken to generalize Equation 3.2 for a heterogeneous array.

For a transit telescope, the visibilities V_ν^{ij} are a periodic function of sidereal time.[2] Therefore, it is a natural operation to compute the Fourier transform of the visibilities with respect to sidereal time $\phi \in [0, 2\pi)$.

$$V_{m,\nu}^{ij} = \int_0^{2\pi} V_\nu^{ij}(\phi) \exp\left(-im\phi \right) \mathrm{d}\phi \tag{3.4}$$

The output of this Fourier transform is the set of m-modes $V_{m,\nu}^{ij}$ where $m = 0, \pm 1, \pm 2, \ldots$ is the Fourier conjugate variable to the sidereal time. The m-mode corresponding to $m = 0$ is a simple average of the visibilities over sidereal time. Similarly, $m = 1$ corresponds to the component of the visibilities that varies over half-day timescales. Larger values of m correspond to components that vary on quicker timescales.

Shaw et al. (2014, 2015) showed that there is a discrete linear relationship between the measured m-modes $V_{m,\nu}^{ij}$ and the spherical harmonic coefficients of the sky brightness $a_{lm,\nu}$.

$$V_{m,\nu}^{ij} = \sum_l B_{lm,\nu}^{ij} a_{lm,\nu} \,, \tag{3.5}$$

where the transfer coefficients $B_{lm,\nu}^{ij}$ are computed from the spherical harmonic transform of the baseline transfer function defined by Equation 3.3. These transfer coefficients define the interferometer's response to the corresponding spherical harmonic coefficients.

Equation 3.5 can be recognized as a matrix equation, where the transfer matrix $\boldsymbol{B}$ is

[2] This is not strictly true. Ionospheric fluctuations and non-sidereal sources (such as the Sun) will violate this assumption. This paper will, however, demonstrate that the impact on the final maps is mild.

block-diagonal:

$$\overbrace{\begin{pmatrix} \vdots \\ m\text{-modes} \\ \vdots \end{pmatrix}}^{\boldsymbol{v}} = \overbrace{\begin{pmatrix} \ddots & & \\ & \text{transfer matrix} & \\ & & \ddots \end{pmatrix}}^{\boldsymbol{B}} \overbrace{\begin{pmatrix} \vdots \\ a_{lm} \\ \vdots \end{pmatrix}}^{\boldsymbol{a}} \tag{3.6}$$

$$\boldsymbol{B} = \begin{pmatrix} m=0 & & & \\ & m=\pm 1 & & \\ & & m=\pm 2 & \\ & & & \ddots \end{pmatrix} \tag{3.7}$$

The vector $\boldsymbol{v}$ contains the list of m-modes and the vector $\boldsymbol{a}$ contains the list of spherical harmonic coefficients representing the sky brightness. In order to take advantage of the block-diagonal structure in $\boldsymbol{B}$, $\boldsymbol{v}$ and $\boldsymbol{a}$ must be sorted by the absolute value of m. Positive and negative values of m are grouped together because the brightness of the sky is real-valued, and the spherical harmonic transform of a real-valued function has $a_{l(-m)} = (-1)^m a^*_{lm}$.

In practice, we now need to pick the set of spherical harmonics we will use to represent the sky. For an interferometer like the OVRO-LWA with many short baselines, a sensible choice is to use all spherical harmonics with $l \leq l_{\text{max}}$ for some l_{max}. The parameter l_{max} is determined by the maximum baseline length of the interferometer. For an interferometer without short spacings, a minimum value for l might also be used. This l_{min} parameter should be determined by the minimum baseline length. A rough estimate of l for a baseline of length b at frequency ν is $l \sim \pi b\nu/c$. Based on this estimate for the OVRO-LWA and other computational considerations, we therefore adapt $l_{\text{min}} = 1$ and $l_{\text{max}} = 1000$ across all frequencies. However, this choice of l_{max} actually limits the angular resolution above 55 MHz, and therefore future work will increase l_{max} to obtain better angular resolution.

The interferometer's sensitivity to the monopole (a_{00}) deserves special consideration. Venumadhav et al. (2016) proveed – under fairly general assumptions – that a baseline with nonzero sensitivity to a_{00} must also have some amount of cross-talk or common-mode noise. In fact, the sensitivity to a_{00} is proportional to a sum of these effects. For example, one way a baseline can have nonzero sensitivity to a_{00} is if the baseline is extremely short. In this case, the antennas are so close together that voltage fluctuations in one antenna can couple into the other antenna. In order to make an interferometric measurement of a_{00}, this coupling must be measured and calibrated. Consequently, we set $a_{00} = 0$ in our analysis. In the future, this limitation will be addressed with the inclusion of calibrated total power radiometry.

The size of a typical block in the transfer matrix is $(2N_{\text{base}}N_{\text{freq}}) \times (l_{\text{max}})$. If each element of the matrix is stored as a 64 bit complex floating point number, a single block is 500 MB for the case of single-channel imaging with the OVRO-LWA, which a modern computer can easily store and manipulate in memory. However, with additional bandwidth, these blocks quickly become unwieldy; thus, as a first pass, the analysis in this paper is restricted to single-channel imaging. Note also that for the OVRO-LWA, $N_{\text{base}} \gg l_{\text{max}}$, so there are more measurements than unknowns in Equation 3.6.

The key advantage of m-mode analysis is the block-diagonal structure of Equation 3.6. The computational complexity of many common matrix operations (e.g., solving a linear system of equations) is $O(N^3)$, where N is the linear size of the matrix. By splitting the equation into M independent blocks, the number of floating point operations required to solve the linear system of equations is now $O(N^3 M^{-2})$, because each block can be manipulated independently of the other blocks. This computational savings is what makes this matrix algebra approach to interferometric imaging feasible. For the data set presented in this paper, computing the elements of the transfer matrix takes ~10 hours per frequency channel on a 10-node cluster, but once the matrix has been computed, the imaging process described in §3.2 takes ~10 minutes, and the deconvolution process described in §3.2 was allowed to run for ~10 hours.

m-mode Analysis Imaging

Imaging in m-mode analysis essentially amounts to inverting Equation 3.6 to solve for the spherical harmonic coefficients $\boldsymbol{a}$. The linear least-squares solution, which minimizes $\|\boldsymbol{v} - \boldsymbol{B}\boldsymbol{a}\|^2$, is given by

$$\hat{\boldsymbol{a}}_{\text{LLS}} = (\boldsymbol{B}^*\boldsymbol{B})^{-1}\boldsymbol{B}^*\boldsymbol{v}\,, \tag{3.8}$$

where * indicates the conjugate-transpose.

However, usually one will find that $\boldsymbol{B}$ is not full rank, and hence $\boldsymbol{B}^*\boldsymbol{B}$ is not an invertible matrix. For example, an interferometer located in the northern hemisphere will never see a region of the southern sky centered on the southern celestial pole. The m-modes contained in the vector $\boldsymbol{v}$ must contain no information about the sky around the southern celestial pole, and therefore the act of multiplying by $\boldsymbol{B}$ must destroy some information about the sky. The consequence of this fact is that $\boldsymbol{B}$ must have at least one singular value that is equal to zero. It then follows that $\boldsymbol{B}^*\boldsymbol{B}$ must have at least one eigenvalue that is equal to zero, which means it is not an invertible matrix.

Another way of looking at the problem is that because the interferometer is not sensitive to part of the southern hemisphere, there are infinitely many possible solutions to Equation 3.6 that will fit the measured data equally well. We will therefore regularize the problem and apply an additional constraint that prefers a unique yet physically reasonable solution.

Tikhonov Regularization

The process of Tikhonov regularization minimizes $\|\boldsymbol{v} - \boldsymbol{B}\boldsymbol{a}\|^2 + \varepsilon\|\boldsymbol{a}\|^2$ for some arbitrary value of $\varepsilon > 0$ chosen by the observer. The solution that minimizes this expression is given by

$$\hat{\boldsymbol{a}}_{\text{Tikhonov}} = (\boldsymbol{B}^*\boldsymbol{B} + \varepsilon\boldsymbol{I})^{-1}\boldsymbol{B}^*\boldsymbol{v}\,. \tag{3.9}$$

Tikhonov regularization adds a small value ε to the diagonal of $\boldsymbol{B}^*\boldsymbol{B}$, fixing the matrix's singularity. By using the singular value decomposition (SVD) of the matrix $\boldsymbol{B} = \boldsymbol{U}\boldsymbol{\Sigma}\boldsymbol{V}^*$, Equation 3.9 becomes

$$\hat{\boldsymbol{a}}_{\text{Tikhonov}} = \boldsymbol{V}(\boldsymbol{\Sigma}^2 + \varepsilon\boldsymbol{I})^{-1}\boldsymbol{\Sigma}\boldsymbol{U}^*\boldsymbol{v}\,, \tag{3.10}$$

where

$$\boldsymbol{\Sigma} = \begin{pmatrix} \sigma_1 & & \\ & \sigma_2 & \\ & & \ddots \end{pmatrix}.$$

The diagonal elements of $\boldsymbol{\Sigma}$ are the singular values of $\boldsymbol{B}$. The contribution of each singular component to the Tikhonov-regularized solution is scaled by $\sigma_i/(\sigma_i^2 + \varepsilon)$, where σ_i is the singular value for the ith singular component. Tikhonov regularization therefore acts to suppress any component for which $\sigma_i \lesssim \sqrt{\varepsilon}$. If $\sigma_i = 0$, the component is set to zero.

In practice, the measurement $\boldsymbol{v}$ is corrupted by noise with covariance $\boldsymbol{N}$. For illustrative purposes, we will assume that $\boldsymbol{N} = n\boldsymbol{I}$ for some $n > 0$. In this case, the covariance of the Tikhonov-regularized spherical harmonic coefficients is

$$\boldsymbol{C} = n\boldsymbol{V}(\boldsymbol{\Sigma}^2 + \varepsilon\boldsymbol{I})^{-2}\boldsymbol{\Sigma}^2\boldsymbol{V}^*\,. \tag{3.11}$$

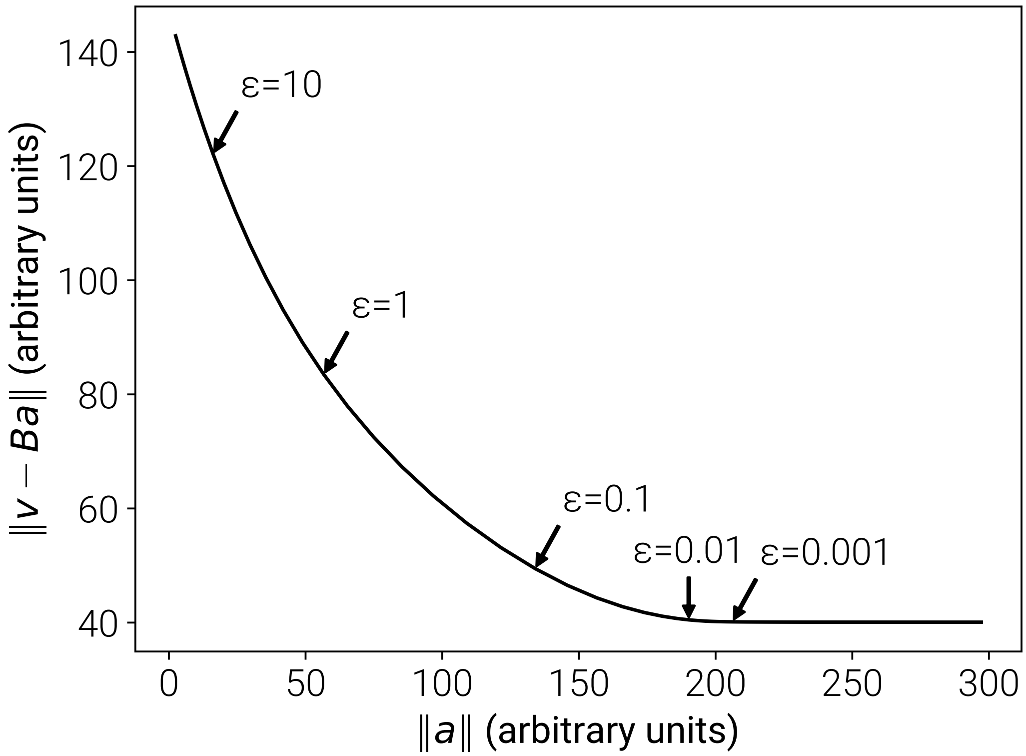

Figure 3.1: Example L curve computed from OVRO-LWA data at 36.528 MHz by trialing 200 different values of the regularization parameter ε. The x-axis is the norm of the solution (in this case, the spherical harmonic coefficients) given in arbitrary units, and the y-axis is the least-squares norm given in arbitrary units. Where the regularization parameter is small, the norm of the solution grows rapidly. Where the regularization parameter is large, the least-squares norm grows rapidly.

Each singular component is scaled by a factor of $\sigma_i^2/(\sigma_i^2+\varepsilon)^2$. In the absence of Tikhonov regularization ($\varepsilon = 0$), singular components with the smallest singular values – the ones that the interferometer is the least sensitive to – actually come to dominate the covariance of the measured spherical harmonic coefficients. Tikhonov regularization improves this situation by down-weighting these components.

L Curves

Tikhonov regularization requires the observer to pick the value of ε. If ε is too large, then too much importance is placed on minimizing the norm of the solution and the least-squares residuals will suffer. Conversely, if ε is too small, then the problem will be poorly regularized and the resulting sky map may not represent the true sky. Picking the value of ε therefore requires understanding the trade-off between the two norms.

This trade-off can be analyzed quantitatively by trialing several values of ε, and computing $\|\boldsymbol{v} - \boldsymbol{B}\boldsymbol{a}\|^2$ and $\|\boldsymbol{a}\|^2$ for each trial. An example is shown in Figure 3.1. The shape of this curve has a characteristic L shape, and as a result, this type of plot is called an L curve. The ideal value of ε lies near the turning point, of the plot. At this point a small decrease in ε will lead to an undesired rapid increase in $\|\boldsymbol{a}\|^2$, and a small increase in ε will lead to an undesired rapid increase in $\|\boldsymbol{v} - \boldsymbol{B}\boldsymbol{a}\|^2$.

In practice, the L curve should be used as a guide to estimate a reasonable value of ε. However, better results can often be obtained by tuning the value of ε. For instance, increasing the value of ε can improve the noise properties of the map by down-weighting noisy modes. Decreasing the value of ε can improve the resolution of the map by up-weighting the contribution of longer baselines, which are likely fewer in number. In this respect, choosing the value of ε is analogous to picking the weighting scheme in traditional imaging where robust weighting schemes can be tuned to similar effect (Briggs, 1995). For the OVRO-LWA, we selected $\varepsilon = 0.01$ across all frequency channels. The distribution of singular values of the transfer matrix with respect to $\sqrt{\varepsilon}$ is summarized in Table 3.1.

Other Regularization Schemes

The choice of applying Tikhonov regularization to m-mode analysis imaging is not unique. There exists a plethora of alternative regularization schemes that could also be applied. Each regularization scheme has its own advantages and disadvantages. For instance, Tikhonov regularization is simple, independent of prior information, and sets unmeasured modes to zero (a sensible expectation). We will now briefly discuss a few other alternatives.

The Moore–Penrose pseudo-inverse (denoted with a superscript †) is commonly applied to find the minimum-norm linear least-squares solution to a set of linear equations. This can be used in place of Tikhonov regularization as

$$\hat{\boldsymbol{a}}_{\text{Moore-Penrose}} = \boldsymbol{B}^{\dagger}\boldsymbol{v}\,. \tag{3.12}$$

Much like Tikhonov regularization, the Moore–Penrose pseudo-inverse sets components with small singular values (below some user-defined threshold) to zero. Components with large singular values (above the user-defined threshold) are included in the calculation at their full amplitude with no down-weighting of modes near the threshold. The essential difference between using the Moore–Penrose pseudo-inverse and Tikhonov regularization is that the pseudo-inverse defines a hard transition from "on" to "off." Modes are either set to zero or included in the map at their full amplitude. On the other hand, Tikhonov regularization smoothly interpolates between these behaviors. Because of this, Tikhonov regularization tends to produce better results in practical applications.

If the measured m-modes have a noise covariance matrix $\boldsymbol{N} \neq n\boldsymbol{I}$ for some scalar n (e.g., the interferometer is inhomogeneous), then the observer should minimize $(\boldsymbol{v} - \boldsymbol{B}\boldsymbol{a})^* \boldsymbol{N}^{-1}(\boldsymbol{v} - \boldsymbol{B}\boldsymbol{a}) + \varepsilon\|\boldsymbol{a}\|^2$. The noise covariance matrix $\boldsymbol{N}$ is used to weight the measurements such that

$$\hat{\boldsymbol{a}}_{\text{min variance}} = (\boldsymbol{B}^*\boldsymbol{N}^{-1}\boldsymbol{B} + \varepsilon\boldsymbol{I})^{-1}\boldsymbol{B}\boldsymbol{N}^{-1}\boldsymbol{v}\,. \tag{3.13}$$

In the event that the observer has a prior map of the sky, $\|\boldsymbol{a} - \boldsymbol{a}_{\text{prior}}\|^2$ can be used as the regularizing norm. This will use the prior map to fill in missing information instead of setting these modes to zero. In this case, the minimum is at

$$\hat{\boldsymbol{a}}_{\text{with prior}} = (\boldsymbol{B}^*\boldsymbol{B} + \varepsilon\boldsymbol{I})^{-1}(\boldsymbol{B}^*(\boldsymbol{v} - \boldsymbol{B}\boldsymbol{a}_{\text{prior}})) + \boldsymbol{a}_{\text{prior}}\,. \tag{3.14}$$

If instead the observer has a prior expectation on the covariance of the spherical harmonic coefficients, Wiener filtering can also be used. This technique is demonstrated for simulated measurements by Berger et al. (2016).

Alternatively, we could opt to regularize the problem by enforcing smoothness in the sky maps. In this case, the regularizing norm should be of the form $\|\nabla I(\hat{r})\|^2$, where ∇I is the gradient of the sky brightness in the direction $\hat{r}$. This is actually a generalization of Tikhonov regularization, where the objective function is $\|\boldsymbol{v} - \boldsymbol{B}\boldsymbol{a}\|^2 + \varepsilon\|\boldsymbol{A}\boldsymbol{a}\|^2$ for some matrix $\boldsymbol{A}$. The minimum is at

$$\hat{\boldsymbol{a}}_{\text{generalized}} = (\boldsymbol{B}^*\boldsymbol{B} + \varepsilon\boldsymbol{A}^*\boldsymbol{A})^{-1}\boldsymbol{B}^*\boldsymbol{v}\,. \tag{3.15}$$

Finally, in many machine-learning applications the L_1-norm[3] is used in place of the usual L_2-norm in order to encourage sparsity in the reconstructed signal. Applying this to m-mode analysis imaging would amount to minimizing $\|\boldsymbol{v} - \boldsymbol{B}\boldsymbol{a}\|_2^2 + \varepsilon\|\boldsymbol{a}\|_1$. However, because we have decomposed the sky in terms of spherical harmonics, the vector $\boldsymbol{a}$ is not expected to be sparse. Consequently, the L_1-norm is generally inappropriate for m-mode analysis imaging without an additional change of variables designed to introduce sparsity.

[3] $\|\boldsymbol{a}\|_1 = \sum_i |a_i|$

CLEAN

In traditional radio astronomy imaging, CLEAN (Högbom, 1974) is a physically motivated algorithm that interpolates between measured visibilities on the *uv* plane. In the absence of this interpolation, gaps in the interferometer's *uv* coverage are assumed to be zero, and – in the image plane – sources are convolved with a point spread function (PSF) that is characteristic of the *uv* coverage. Fundamentally, the interferometer's PSF is determined by which modes were assumed to be zero in the initial imaging process.

In m-mode analysis imaging, we assumed modes were zero in two separate ways.

1. We selected a set of spherical harmonic coefficients a_{lm} to describe the sky-brightness distribution. All modes with $l > l_{\max}$ are neglected and assumed to be zero.
2. Tikhonov regularization forces linear combinations of spherical harmonic coefficients with $\sigma_i \lesssim \sqrt{\varepsilon}$ toward zero.

As a consequence, the final map of the sky is not assembled from a complete set of spherical harmonics. Therefore, just as in traditional imaging, m-mode analysis imaging produces dirty maps in which sources are convolved with a PSF. This PSF can be improved by increasing the number and variety of baselines, which increases the number of modes for which $\sigma_i \gg \sqrt{\varepsilon}$. Alternatively, by collecting more data, the signal-to-noise ratio of the measured m-modes increases, which allows the observer to lower the value of ε without increasing the noise in the maps. Finally, the CLEAN algorithm can be applied to interpolate some of the missing information that was assumed to be zero.

The PSF of a dirty m-mode analysis map may be computed with

$$\boldsymbol{a}_{\text{PSF}}(\theta, \phi) = (\boldsymbol{B}^*\boldsymbol{B} + \varepsilon\boldsymbol{I})^{-1}\boldsymbol{B}^*\boldsymbol{B}\boldsymbol{a}_{\text{PS}}(\theta, \phi)\,, \tag{3.16}$$

where $\boldsymbol{a}_{\text{PSF}}(\theta, \phi)$ is the vector of spherical harmonic coefficients representing the PSF at the spherical coordinates (θ, ϕ), and $\boldsymbol{a}_{\text{PS}}(\theta, \phi)$ is the vector of spherical harmonic coefficients for a point source at (θ, ϕ) given by

$$\boldsymbol{a}_{\text{PS}}(\theta, \phi) = \begin{pmatrix} \vdots \\ Y^*_{lm}(\theta, \phi) \\ \vdots \end{pmatrix} = \begin{pmatrix} \vdots \\ Y^*_{lm}(\theta, 0) \times e^{im\phi} \\ \vdots \end{pmatrix}. \tag{3.17}$$

In general, the PSF can be a function of the right ascension and declination. However, point sources at the same declination take the same track through the sky and (barring any ionospheric effects) will have the same PSF. The PSF is therefore only a function of the declination. For example, sources at low elevations will tend to have an extended PSF along the north–south axis due to baseline foreshortening. For the OVRO-LWA antenna configuration (Figure 3.2), example PSFs at three separate frequencies are shown in Figure 3.3. Adapting CLEAN for m-mode analysis requires either precomputing Equation 3.16 at a grid of declinations, or a method for rapidly evaluating Equation 3.16 on the fly.

For an interferometer with more baselines than spherical harmonics used in the maps (e.g., the OVRO-LWA), $\boldsymbol{B}^*\boldsymbol{B}$ can be a much smaller matrix than the full transfer matrix $\boldsymbol{B}$. Therefore, precomputing $\boldsymbol{B}^*\boldsymbol{B}$ can allow the entire matrix to fit into memory on a single machine. This greatly reduces the amount of disk I/O necessary for solving Equation 3.16.

Additionally, we can precompute the Cholesky decomposition of $\boldsymbol{B}^*\boldsymbol{B} + \varepsilon\boldsymbol{I} = \boldsymbol{U}^*\boldsymbol{U}$, where $\boldsymbol{U}$ is an upper triangular matrix. Inverting an upper triangular matrix is an $O(N^2)$ operation (instead of $O(N^3)$ for a general matrix inverse).[4] Equation 3.16 can then be rapidly evaluated from right to left as

$$\boldsymbol{a}_{\mathrm{PSF}} = \boldsymbol{U}^{-1}\left(\boldsymbol{U}^*\right)^{-1}\left(\boldsymbol{B}^*\boldsymbol{B}\right)\boldsymbol{a}_{\mathrm{PS}}\,. \tag{3.18}$$

Furthermore, Equation 3.18 does not need to be separately evaluated for each CLEAN component. Instead, we can identify N CLEAN components, accumulate $\boldsymbol{a}_{\mathrm{PS}}$ for each component, and evaluate Equation 3.18 on the accumulation. This can greatly reduce the number of times this equation needs to be evaluated, but care must be taken to ensure that the N components are not so close together that sidelobes from one may interact with another.

Altogether, the adaptation of CLEAN applied to the maps presented in this paper is summarized below.

Precondition: $\boldsymbol{a}$ is the solution to Equation 3.9

function CLEAN($\boldsymbol{a}$)
    $\boldsymbol{M} \leftarrow \boldsymbol{B}^*\boldsymbol{B}$
    $\boldsymbol{U} \leftarrow chol(\boldsymbol{M} + \varepsilon\boldsymbol{I})$ ▹ Cholesky decomposition
    while noise in map > threshold **do**

[4] Instead of computing $\boldsymbol{A}^{-1}$, we solve the linear equation $\boldsymbol{Ax} = \boldsymbol{b}$ each time the matrix inverse is needed so as to avoid numerical instabilities.

find N pixels with the largest residual flux
$\boldsymbol{x} \leftarrow \sum_{i=1}^{N} (\text{pixel flux}) \times \boldsymbol{a}_{\text{PS}}(\theta_i, \phi_i)$
$\boldsymbol{y} \leftarrow \boldsymbol{U}^{-1} \left(\boldsymbol{U}^*\right)^{-1} \boldsymbol{M}\boldsymbol{x}$
$\boldsymbol{a} \leftarrow \boldsymbol{a} - (\text{loop gain}) \times \boldsymbol{y}$
record subtracted components
$\boldsymbol{a} \leftarrow \boldsymbol{a} + (\text{restored components})$
return $\boldsymbol{a}$

In summary, Tikhonov-regularized m-mode analysis imaging constructs a wide-field synthesis image of the sky from a complete Earth rotation, and with exact treatment of wide-field effects. This is accomplished by solving a regularized block-diagonal matrix equation (Equation 3.9). The solution to this equation generates a map where sources are convolved with a PSF characteristic of the interferometer (a function of the frequency, antenna response, and baseline distribution with a full Earth rotation). The CLEAN algorithm is adopted to deconvolve the PSF and produce the final sky maps.

3.3 Observations

The OVRO-LWA

The OVRO-LWA is a 288-element interferometer located at OVRO near Big Pine, California (Hallinan et al., in prep.). The OVRO-LWA is a low-frequency instrument with instantaneous bandwidth covering 27 to 85 MHz and with 24 kHz channelization. Each antenna stand hosts two perpendicular broadband dipoles so that there are 288×2 signal paths in total. These signal paths feed into the 512-input LEDA correlator (Kocz et al., 2015), which allows the OVRO-LWA to capture the entire visible hemisphere in a single snapshot image.

The 288 antennas are arranged in a pseudo-random configuration optimized to minimize sidelobes in snapshot imaging (see Figure 3.2). Of these 288 antennas, 251 are contained within a 200 m diameter core, 32 are placed outside of the core in order to extend the maximum baseline length to $\sim$1.5 km, and five are equipped with noise-switched front ends for calibrated total power measurements of the global sky brightness. These antennas are used as part of the LEDA experiment (Price et al., 2017) to measure the global signal of 21 cm absorption from the cosmic dawn. In the current configuration, 32 antennas (64 signal paths) from the core are disconnected from the correlator in order to accommodate the 32 antennas on longer baselines. A final stage of construction will involve 64 additional antennas installed on long

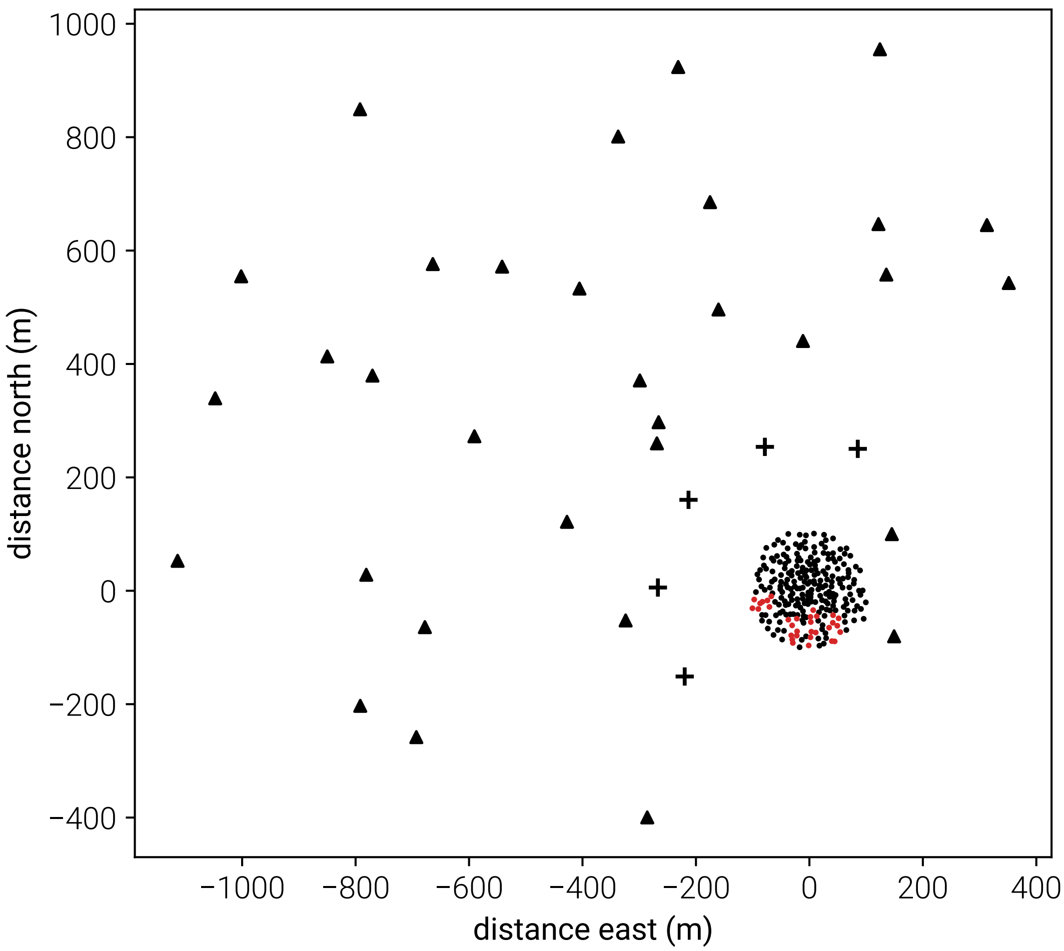

Figure 3.2: Antenna layout for the OVRO-LWA. Black dots correspond to antennas within the 200 m diameter core of the array. The 32 triangles are the expansion antennas built in early 2016 in order to increase the longest baseline to ∼ 1.5 km. The red dots are core antennas that are disconnected from the correlator in order to accommodate these antennas. The five crosses are antennas equipped with noise-switched front ends.

baselines out to a maximum length of 2.6 km.

The data set used in this paper spans 28 consecutive hours beginning at 2017 February 17 12:00:00 UTC time. During this time, the OVRO-LWA operated as a zenith-pointing drift-scanning interferometer. The correlator dump time was selected to be 13 s such that the correlator output evenly divides a sidereal day. Due to the computational considerations presented in §3.2, eight 24 kHz channels are selected for imaging from this data set: 36.528, 41.760, 46.992, 52.224, 57.456, 62.688, 67.920, and 73.152 MHz. These particular channels are chosen due to their location at the exact center of instrumental subbands.

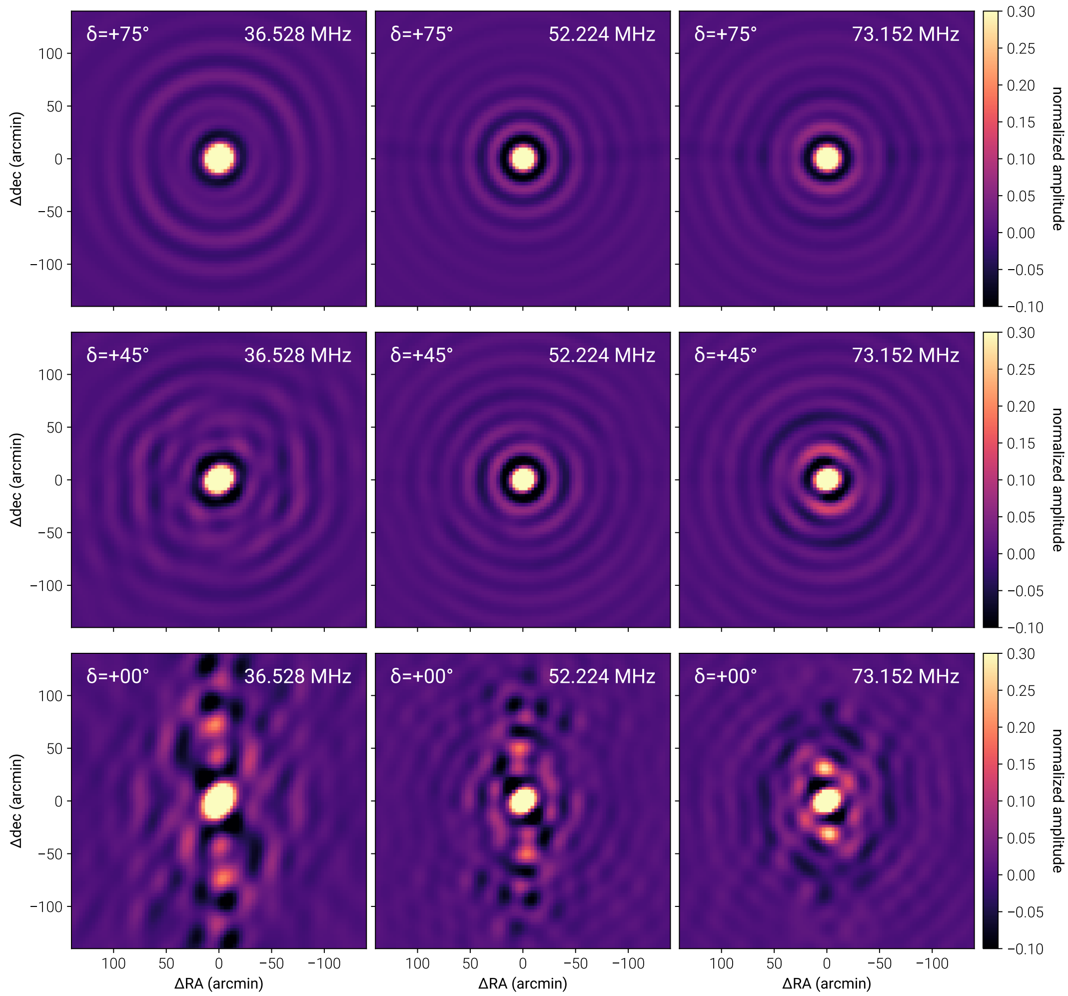

Figure 3.3: The m-mode analysis imaging PSF at three declinations (top row: $\delta = +75°$, middle row: $\delta = +45°$, bottom row: $\delta = +0°$) and three frequencies (left column: 36.528 MHz, middle column: 52.224 MHz, right column: 73.152 MHz). The PSF is computed by evaluating Equation 3.16. Above 55 MHz, the angular extent of the PSF does not follow the expected scaling with frequency because the angular resolution is limited by the selection of $l_{max} = 1000$. The FWHM at $\delta = +45°$ is listed in Table 3.1.

Complex Gain Calibration

The complex gain calibration is responsible for correcting per-antenna amplitude and phase errors. This is accomplished using a sky model and a variant of alternating least-squares colloquially known as "Stefcal" (Mitchell et al., 2008; Salvini & Wijnholds, 2014)[5].

[5] The calibration routine is written in the Julia programming language (Bezanson et al., 2017), and is publicly available online (`https://github.com/mweastwood/TTCal.jl`) under an open source license (GPLv3 or any later version).

Cyg A and Cas A are – by an order of magnitude – the brightest point-like radio sources in the northern hemisphere at resolutions lower than 0.25°. Therefore, the optimal time to solve for the interferometer's gain calibration is when these sources are at high elevations. The antenna complex gains are measured from a 22 minute track of data when Cyg A and Cas A are at high elevations. The gains measured in this way are then used to calibrate the entire 28 hour data set. The calibration sky model consists only of Cyg A and Cas A. The model flux of Cyg A is set to the Baars et al. (1977) spectrum, while the flux of Cas A is measured from the data itself (using a preliminary calibration solved for with a fiducial Cas A spectrum).

Calibrating in this manner generates approximately arcminute errors in the astrometry of the final sky maps due to ionospheric refractive offsets during the time of calibration. These residual errors in the astrometry are corrected post-imaging by registering the images with respect to all Very Large Array Low-frequency Sky Survey Redux (VLSSr) (Lane et al., 2014) sources that are bright (> 30 Jy with a consistent flux density measured with the OVRO-LWA) and not too close to other bright sources (at least 1° separation).

Temperature fluctuations of the analog electronics generate 0.1 dB sawtooth oscillations in the analog gain. These oscillations occur with a variable 15 to 17 minute period associated with HVAC cooling cycles within the electronics shelter that houses these electronics. The amplitude of these gain fluctuations is calibrated by smoothing the autocorrelation amplitudes on 45 minute timescales. The ratio of the measured autocorrelation power to the smoothed autocorrelation power defines a per-antenna amplitude correction that is then applied to the cross-correlations. Additionally, the ambient temperature at the front-end electronics (located in a box at the top of each dipole) fluctuates diurnally, which will generate diurnal gain fluctuations. At this time, no correction is made for these diurnal gain fluctuations.

Primary Beam Measurements

In order to generate wide-field images of the sky, the response of the antenna to the sky must be known. Drift-scanning interferometers like the OVRO-LWA can empirically measure their primary beam under a mild set of symmetry assumptions (Pober et al., 2012). The symmetry assumptions are necessary to break the degeneracy between source flux and beam amplitude when the flux of the source is unknown. In this work, we assume symmetries that are apparent in the antenna design, but real-world defects and coupling with nearby antennas will contribute

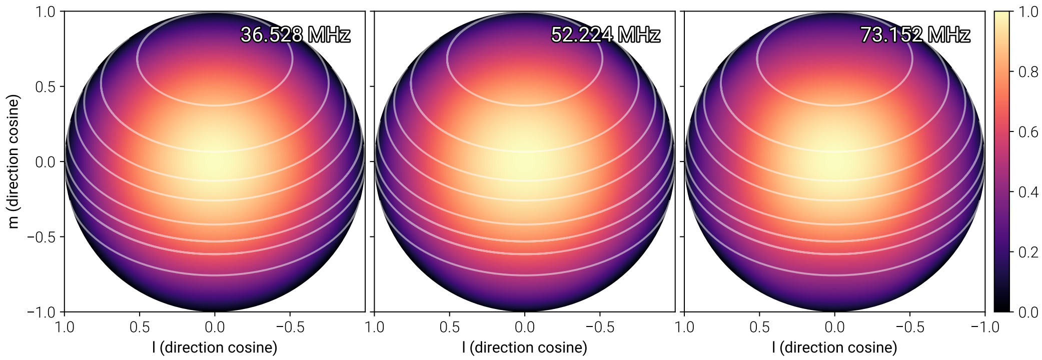

Figure 3.4: Empirical fits to the OVRO-LWA Stokes I primary beam (the response of the x and y dipoles has been summed) at three frequencies: 36.528 MHz (left panel), 52.224 MHz (middle panel), and 73.152 MHz (right panel). The source tracks used to measure the beam model are overlaid. From north to south, these tracks correspond to Cas A, Cyg A, 3C 123, Tau A, Vir A, Her A, 3C 353, and Hya A. The fitting process is described in §3.3, and residuals for Cyg A and Cas A are in Figure 3.5.

toward breaking these symmetries at some level. In particular, we assume that the x and y dipoles have the same response to the sky after rotating one by 90°, and that the beam is invariant under north–south and east–west flips.

We measure the flux of several bright sources (Cyg A, Cas A, Tau A, Vir A, Her A, Hya A, 3C 123, and 3C 353) as they pass through the sky and then fit a beam model composed of Zernike polynomials to those flux measurements. We select the basis functions to have the desired symmetry (Z_0^0, Z_2^0, Z_4^0, Z_4^4, Z_6^0, Z_6^4, Z_8^0, Z_8^4, and Z_8^8), and the beam amplitude at zenith is constrained to be unity. See Figure 3.4 for an illustration of a fitted beam model at several frequencies. This process is repeated for each frequency channel. Residuals for Cyg A and Cas A can be seen in Figure 3.5.

Ionospheric Conditions

The geomagnetic conditions during this time were mild. The Disturbance storm time (Dst) index, which measures the z-component of the interplanetary magnetic field, was > -30 nT during the entirety of the observing period.[6] Following the classification scheme of Kintner et al. (2008), a weak geomagnetic storm has Dst < -30 nT. Stronger geomagnetic storms have Dst < -50 nT.

Despite the mild conditions, low-frequency interferometric observations are still affected by the index of refraction in the ionosphere. Figure 3.6 shows the median

[6] The Dst index was obtained from the World Data Center for Geomagnetism, Kyoto University (`http://swdcwww.kugi.kyoto-u.ac.jp/`). Accessed 2017 July 25.

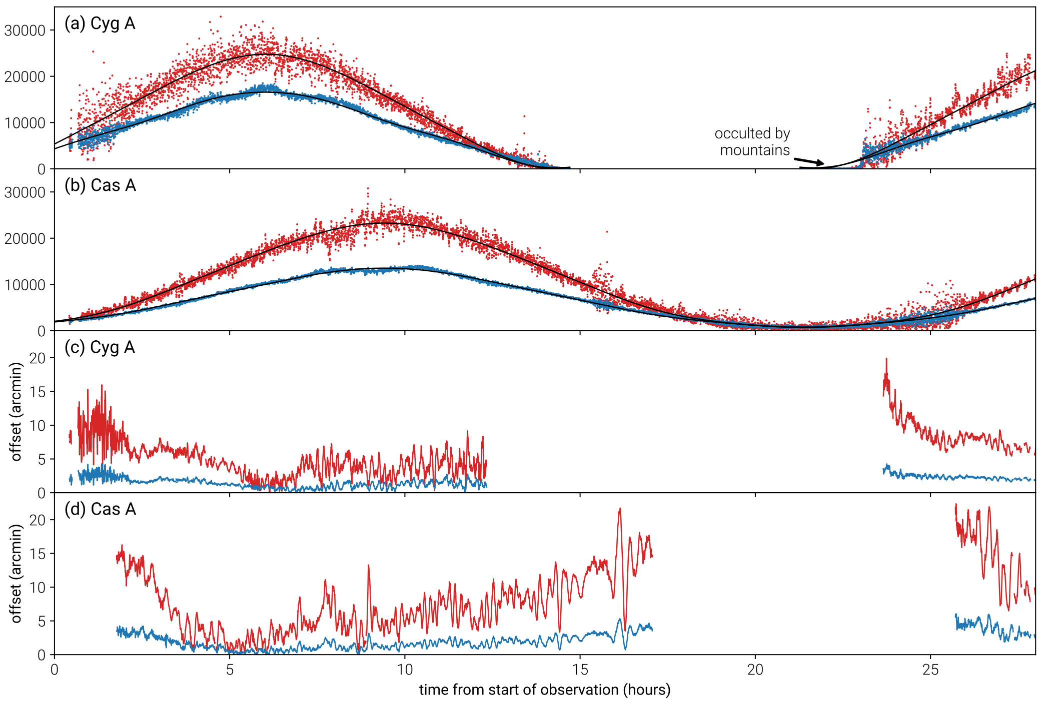

Figure 3.5: Panels (a) and (b) show the measured apparent flux of Cyg A and Cas A at 36.528 MHz (red points) and 73.152 MHz (blue points) as a function of time over the observing period. The solid black curves show the expected flux computed using the empirical beam model fits. The thermal noise contribution to each point is about 50 Jy. Cyg A is occulted by the White Mountains when it is low on the horizon to the east. Panels (c) and (d) show the measured position offset of Cyg A and Cas A relative to their true astronomical positions at 36.528 MHz (red line) and 73.152 MHz (blue line).

vertical total electron content (TEC) above OVRO measured from GPS (Iijima et al., 1999). The median is computed over all GPS measurements within 200 km of the observatory. Over the observing period, the TEC smoothly varies from 20 TECU at midday to 5 TECU during the night. However, this measurement is only sensitive to large-scale fluctuations in the ionosphere and does not capture small-scale fluctuations.

Small-scale fluctuations are best characterized by source scintillation and refractive offsets. Figure 3.5 shows the apparent flux and position offset of Cyg A and Cas A as a function of time over the entire observing period. Both sources exhibit rapid scintillation on the timescale of a single integration (13 s). For example, at 36.528 MHz, it is not unusual for Cyg A to have measured flux variations of 50% between adjacent 13 second integrations. The variance at 36.528 MHz compared with the variance at 73.152 MHz is consistent with an ionospheric ν^{-2} origin. The

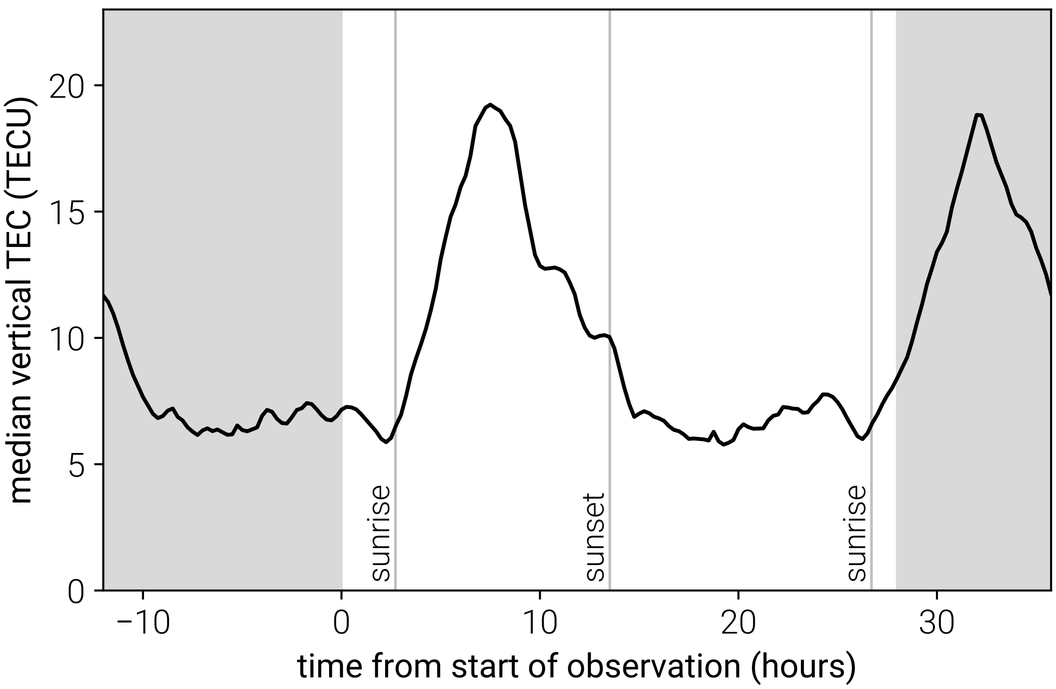

Figure 3.6: Median vertical TEC within 200 km of OVRO during the time of the observation. The gray shaded regions indicate times outside of the observing period. The gray vertical lines indicate sunrise and sunset (as labeled).

measured position offset of each source is a measurement of the ionospheric phase gradient across the array. This varies on slower 10 minute timescales, with each source refracting by as much as 20′(at 36.528 MHz) from its true astronomical position as waves in the ionosphere pass through the line of sight. At 74 MHz on the VLA, Kassim et al. (2007) observed $\sim 1'$ refractive offsets during the night, and $\sim 4'$ offsets during the day on similar ~ 10 minute timescales, which is consistent with what is seen here. The impact of these effects on the sky maps is simulated in §3.5.

Source Removal

Cyg A and Cas A

Due to the rapid and large ionospheric fluctuations seen in Figure 3.5, CLEAN cannot be relied on to accurately deconvolve bright sources. However, without removing bright sources from the data, sidelobes from these sources will dominate the variance in the sky maps. At 74 MHz, Cyg A is a 15,000 Jy source (Baars et al., 1977). A conservative estimate for the confusion limit at 74 MHz with a 15′beam is 1000 mJy (Lane et al., 2014). Therefore, we require that Cyg A's sidelobes be at least −45 dB down from the main lobe to prevent Cyg A's sidelobes from dominating the variance in the image.

To achieve this dynamic range at low frequencies, it is important to account for propagation effects through the ionosphere. In the weak scattering regime ($r_\text{diff} \gg r_\text{f}$, where r_diff is the diffractive scale of the ionosphere, $r_\text{f} = \sqrt{\lambda D/2\pi}$ is the Fresnel scale, λ is the wavelength, and D is the distance to the ionosphere), fluctuations within the ionosphere contribute amplitude and phase scintillations that can be described by a direction-dependent complex gain calibration. This justifies the use of "peeling," which incorporates a direction-dependent calibration to subtract sources in the presence of ionospheric scintillation (e.g., Mitchell et al., 2008; Smirnov & Tasse, 2015).

In the strong scattering regime ($r_\text{diff} \lesssim r_\text{f}$), the image of a point source can "break apart" into multiple images or speckles (Vedantham & Koopmans, 2015). Attempting to peel a source in the strong scattering regime will lead to source-subtraction artifacts in the final sky map. Mevius et al. (2016) measured that from the location of LOFAR at 150 MHz, the diffractive scale of the ionosphere is > 5 km 90% of the time. This implies that at 73 MHz, the diffractive scale is typically > 2 km, and at 36 MHz, the diffractive scale is typically > 1 km. These limits are comparable to the Fresnel scale for the OVRO-LWA (i.e., $r_\text{diff} > r_\text{f}$), and therefore we do not generally expect to see strong scattering from the ionosphere. Ionospheric conditions during the observing period were mild (see §3.3). However, we do observe scintillation and refractive-offset events on the timescale of a single integration (13 s; see Figure 3.5). Consequently, we peeled Cyg A and Cas A from the data set using a new solution for each integration.

In addition, the largest angular scale of Cas A is $\sim 8'$, and the largest angular scale of Cyg A is $\sim 2'$. With an $\sim 10'$ resolution on its longest baselines at 73 MHz, the OVRO-LWA marginally resolves both sources. A resolved source model is needed for both sources. We fit a self-consistent resolved source model to each source. This is performed by minimizing the variance within an aperture located on each source after peeling. By phasing up a large number of integrations before imaging (at least 1 hour), it is possible to smear out the contribution of the rest of the sky. We then use a nonlinear optimization routine (NLopt Sbplx; Rowan, 1990; Johnson, 2008) to vary the parameters in a source model until the variance within the aperture is minimized. Cyg A is modeled with two Gaussian components, while Cas A is modeled with three Gaussian components. Ultimately, these multicomponent models are used to peel Cyg A and Cas A, but residual errors from this model and from the ionosphere (particularly while these sources are at low elevations) contribute residual artifacts that are largely localized to within $1°$ of each source.

Other Bright Sources

Other bright sources – namely Vir A, Tau A, Her A, Hya A, 3C 123, and 3C 353 – are also removed from the visibilities prior to imaging. Because these sources are much fainter than Cyg A and Cas A, we do not need resolved source models to be able to remove these sources from the visibilities without residual sidelobes contaminating the image.

However, the ionosphere will cause these sources to scintillate and refract. The position and flux of each source is measured separately in each channel and integration. The sources are then subtracted from the visibilities using the updated position and flux of the source. The brightest of these sources (Vir A and Tau A) are peeled using a direction-dependent calibration when they are at high elevations.

The Sun

The Sun can be trivially removed from any map of the sky by constructing the map using only data collected at night. A map of the entire sky can be obtained by using observations spaced 6 months apart. However, the data set used in this paper consists of 28 consecutive hours. Fortunately, the Sun was not active during this period, which could have greatly increased the difficulty involved in subtracting the Sun.

We attempt to subtract the Sun from the data set with the goal of suppressing its sidelobes. The Sun is well-resolved by the OVRO-LWA, and hence a detailed source model is needed. In fact, the optical depth $\tau = 1$ surface of the Sun changes with frequency, and as a consequence, a new model is needed at each frequency. While we could fit a limited number of Gaussian components to Cyg A and Cas A, this is insufficient for the Sun. Additionally, while most astronomical sources at these frequencies have negative spectral indices, the Sun has a positive spectral index. Therefore, more care will need to be taken in subtracting the Sun at higher frequencies than at lower frequencies.

The strategy used for removing the Sun below 55 MHz involves fitting a shapelet (Refregier, 2003) model to the Sun and subtracting without the use of direction-

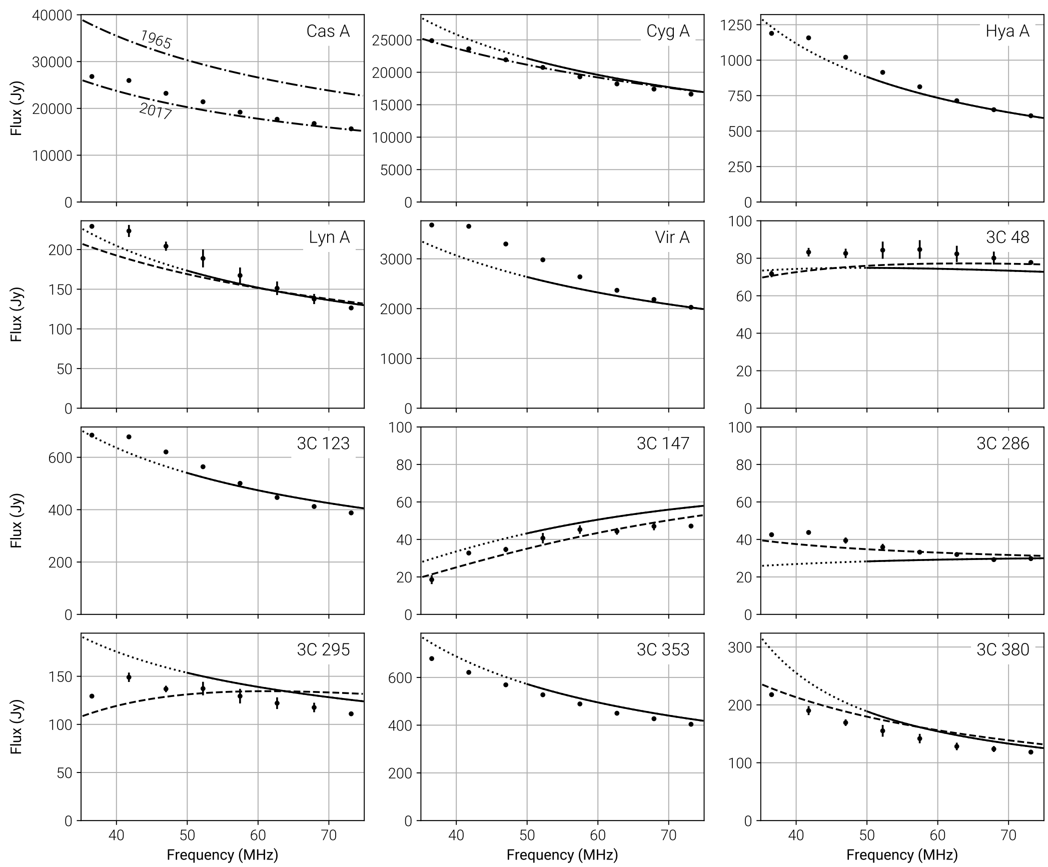

Figure 3.7: Measured fluxes (black points) of 11 sources plotted against the published spectra from Perley & Butler (2017) (solid line above 50 MHz, dotted line below 50 MHz), Scaife & Heald (2012) (dashed line), and Baars et al. (1977) (dot-dashed line). Cas A is compared against a spectrum assuming a secular decrease of 0.77% per year (Helmboldt & Kassim, 2009).

dependent gains. The shapelet fitting is performed in the visibility space. Above 55 MHz, a model is fit to the Sun by minimizing the residuals after peeling (in the same way that models are obtained for Cyg A and Cas A). The Sun is then peeled from each integration using direction-dependent gains.

Flux Scale

The flux scale of the data was tied to the Baars et al. (1977) spectrum of Cyg A during gain calibration. However, gain calibration is also a function of the beam model and the spectrum used for Cas A. Recent work by Scaife & Heald (2012) (hereafter SH12) using archival data from the literature and Perley & Butler (2017) (hereafter PB17) using the VLA has expanded the number of low-frequency radio sources with calibrated flux measurements from one (Cyg A) to 11 in total. While the SH12 flux scale is valid between 30 and 300 MHz, the PB17 flux scale is somewhat more limited because the lowest-frequency observations come from the VLA 4-band system. As a consequence, the PB17 flux scale is not valid below 50 MHz.

Figure 3.7 shows a comparison between flux measurements made using the all-sky maps from this work and spectra from the aforementioned flux scales. Generally, the OVRO-LWA flux measurements agree to between 5% and 10% of the SH12 spectra. Below 50 MHz, there can be substantial departures with respect to the extrapolated PB17 spectra (e.g., 3C 286, 3C 295, and 3C 380), but it is usually the case that we have much better agreement with the SH12 spectra. This indicates that the PB17 spectra cannot be extrapolated below 50 MHz.

3.4 Results

We constructed eight sky maps using Tikhonov-regularized m-mode analysis imaging and CLEANing with observations from the OVRO-LWA. Each map is individually shown in Figure 3.8, Figure 3.9 is a three-color image constructed from the maps at 36.528, 52.224, and 73.152 MHz, and Figure 3.10 is a cutout of the galactic plane. The maps cover the sky north of $\delta = -30°$ with $\sim 15'$ angular resolution. The eight brightest northern hemisphere point sources are removed from each map (Cyg A, Cas A, Vir A, Tau A, Her A, Hya A, 3C 123, and 3C 353), as described in §3.3, and there is a small blank region near $l = +45.7°$, $b = -47.9°$ corresponding to the position of the Sun during the observing window. The properties of each map – including frequency, bandwidth, angular resolution, and thermal noise – are presented in Table 3.1.

Each map from Figure 3.8 will be made freely available online in Healpix format (Górski et al., 2005) on LAMBDA.

Due to the considerations presented by Venumadhav et al. (2016) and discussed in §3.2, each of these maps is monopole-subtracted ($a_{00} = 0$). Furthermore, in order to suppress sources of terrestrial interference, all spherical harmonics with $m = 0$, or $m = 1$ and $l > 100$ are filtered from the map (where the spherical harmonics are defined in the J2017 coordinate system). As will be discussed in §3.5, these spherical harmonics are particularly susceptible to contamination by radio-frequency interference (RFI) and common-mode pickup. As a consequence, astronomical emission that circles the J2017 north celestial pole (NCP) is filtered from the maps. This filtering creates negative rings around the NCP at the declination

	$\boldsymbol{\nu}$	$\boldsymbol{\Delta\nu}$[a]	**FWHM**[b]			**Noise**[c]		**Fraction of Modes**[d]
#	MHz	MHz	$\delta = 0°$	$\delta = +45°$	$\delta = +75°$	K	mJy/beam	with $\sigma > \sqrt{\varepsilon}$
1	36.528	0.024	$26.0' \times 19.1'$	$20.2' \times 16.9'$	$19.8' \times 18.7'$	595.	799.	0.391
2	41.760	0.024	$23.3' \times 17.5'$	$18.5' \times 16.0'$	$18.3' \times 17.4'$	541.	824.	0.480
3	46.992	0.024	$20.9' \times 16.3'$	$17.4' \times 15.2'$	$17.6' \times 16.9'$	417.	717.	0.504
4	52.224	0.024	$18.7' \times 15.2'$	$16.2' \times 15.0'$	$16.0' \times 15.8'$	418.	814.	0.535
5	57.456	0.024	$18.0' \times 14.9'$	$15.9' \times 15.0'$	$15.7' \times 15.4'$	354.	819.	0.542
6	62.688	0.024	$17.8' \times 15.0'$	$15.8' \times 14.9'$	$15.7' \times 15.4'$	309.	843.	0.540
7	67.920	0.024	$17.6' \times 15.0'$	$15.9' \times 14.7'$	$15.8' \times 15.6'$	281.	894.	0.529
8	73.152	0.024	$18.6' \times 15.1'$	$16.8' \times 14.6'$	$16.6' \times 16.1'$	154.	598.	0.512

Table 3.1: A summary of the generated all-sky maps.

[a] Bandwidth used to construct the map. As described in the text, each map is constructed from a single frequency channel (24 kHz).

[b] The full width at half maximum (FWHM) of the synthesized beam at the specified declination (major axis × minor axis).

[c] Measured with a jackknife and splitting the data set into even- and odd-numbered integrations. This estimate therefore includes all noise sources that act on the timescale of a single 13 s integration (e.g., thermal, ionospheric, etc.).

[d] Singular values of the transfer matrix compared with the value of the regularization parameter ε used while solving Equation 3.9. As discussed in the text, singular vectors with corresponding singular values $\sigma \ll \sqrt{\varepsilon}$ are set to zero by the Tikhonov regularization procedure.

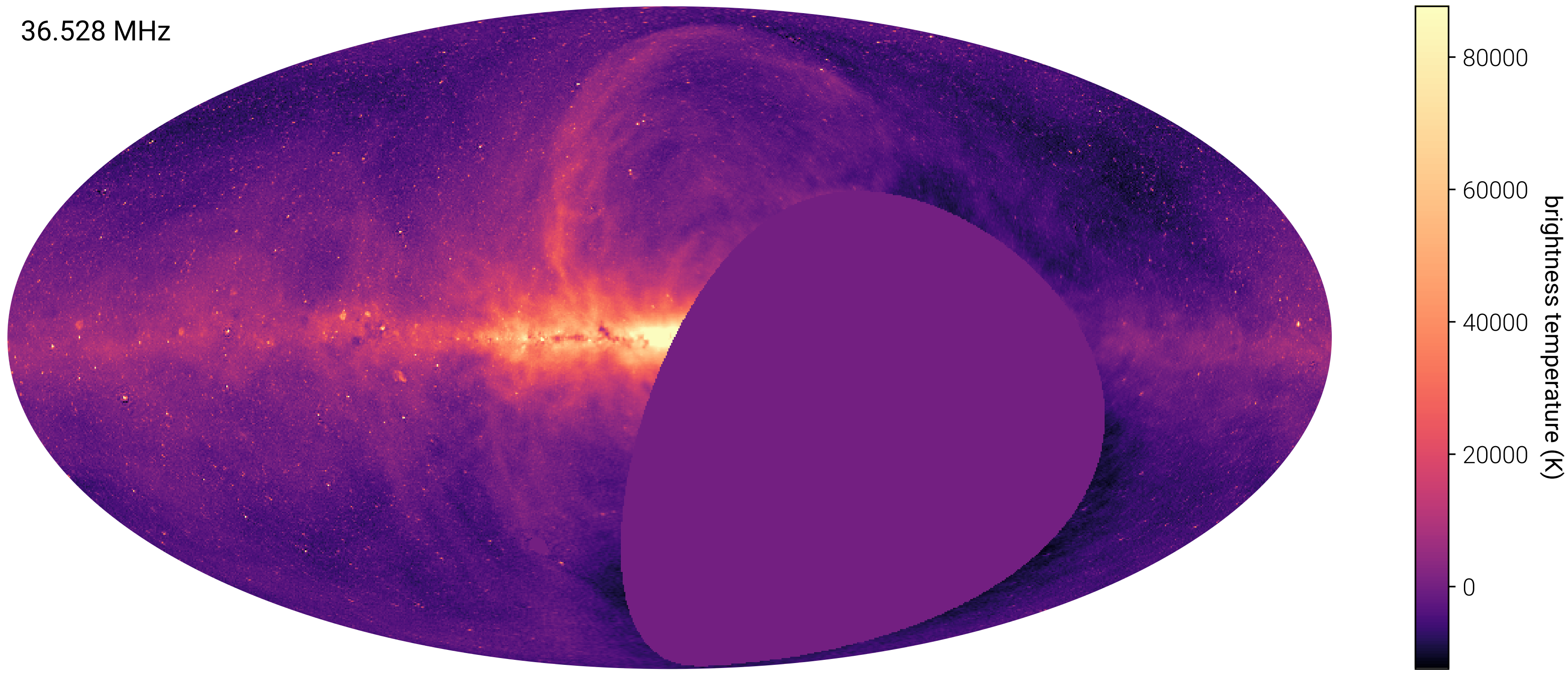

Figure 3.8: These eight panels illustrate (with a Mollweide projection and logarithmic color scale) the eight full-sky maps generated with Tikhonov-regularized m-mode analysis imaging and the OVRO-LWA. Each map covers the sky north of $\delta = -30°$ with angular resolution of $\sim 15'$. Eight bright sources have been removed from each map (Cyg A, Cas A, Vir A, Tau A, Her A, Hya A, 3C 123, and 3C 353). The small blank region near $l = +45.7°$, $b = -47.9°$ corresponds to the location of the Sun during the observation period. A detailed summary of the properties of each map is given in Table 3.1.

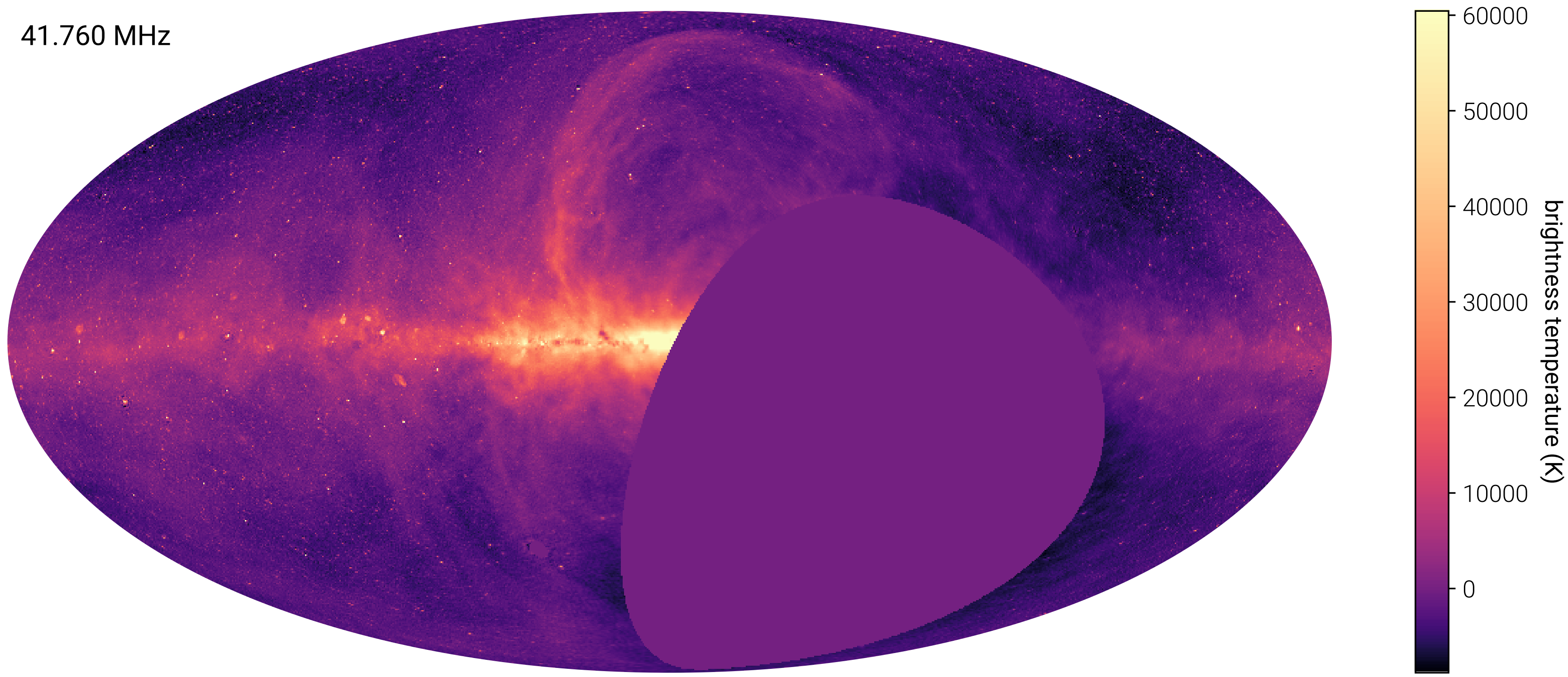

Figure 3.8: continued

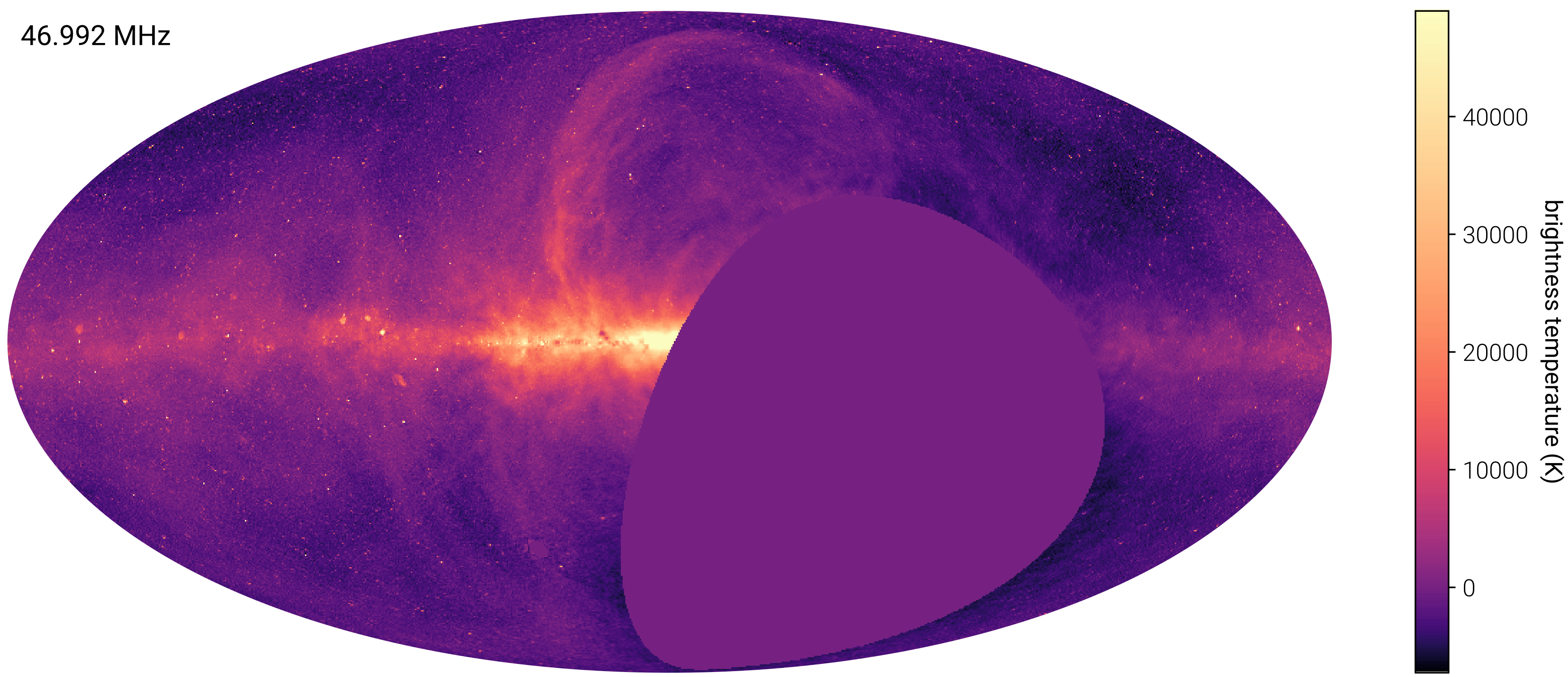

Figure 3.8: continued

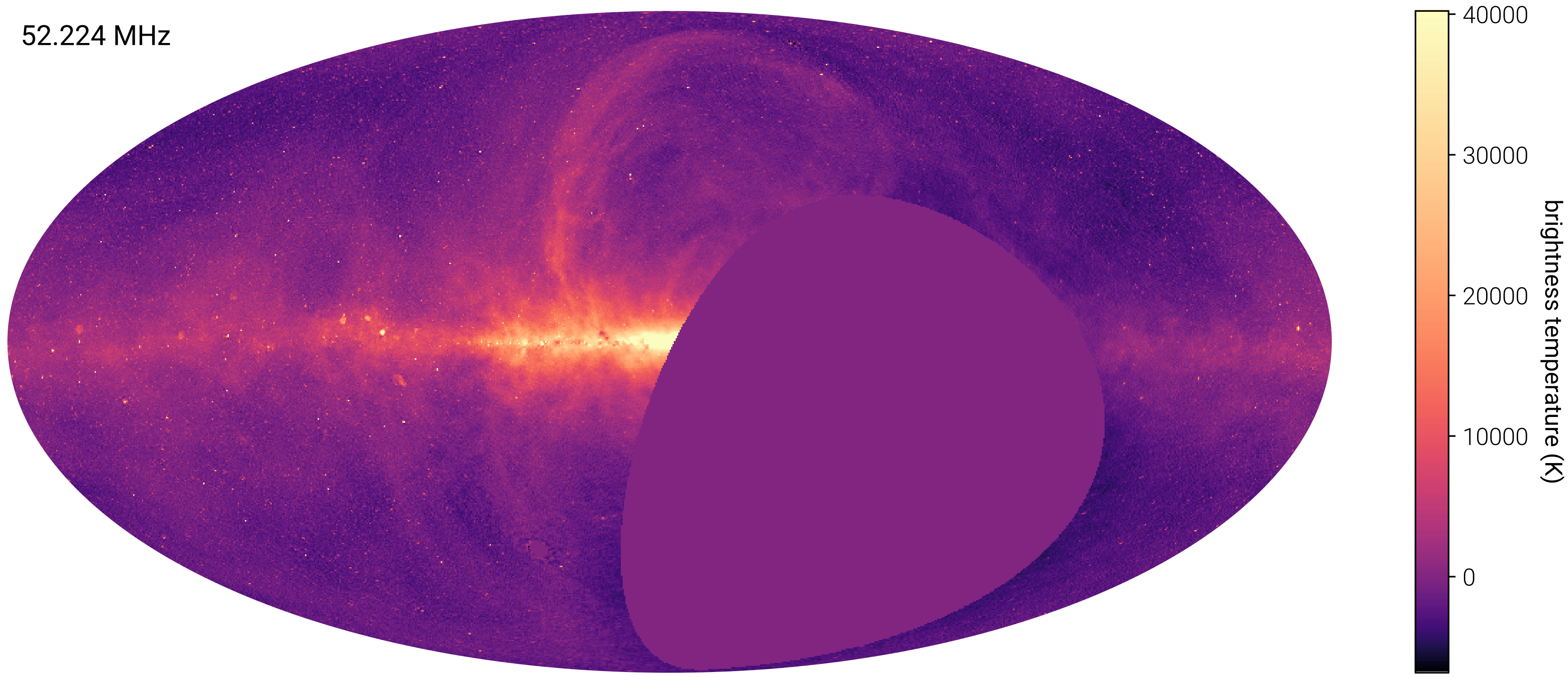

Figure 3.8: continued

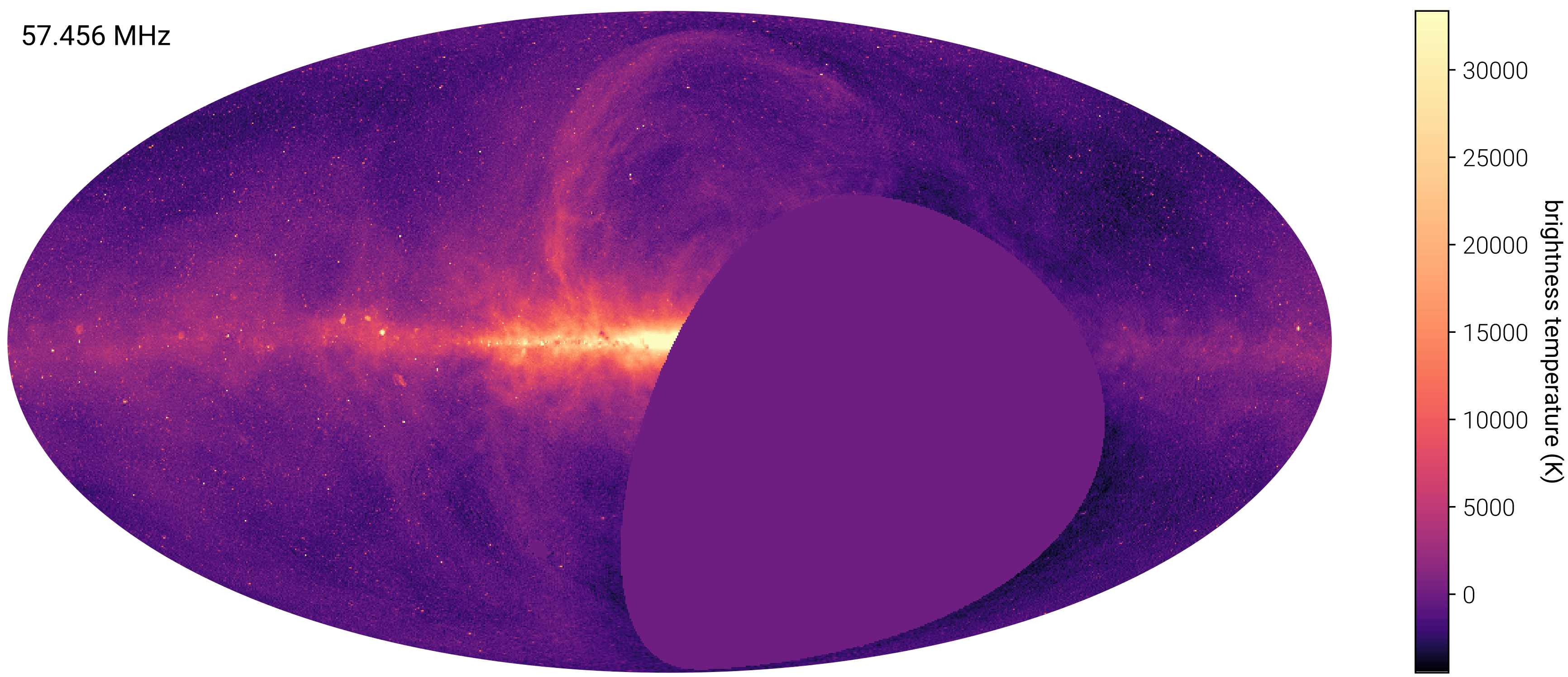

Figure 3.8: continued

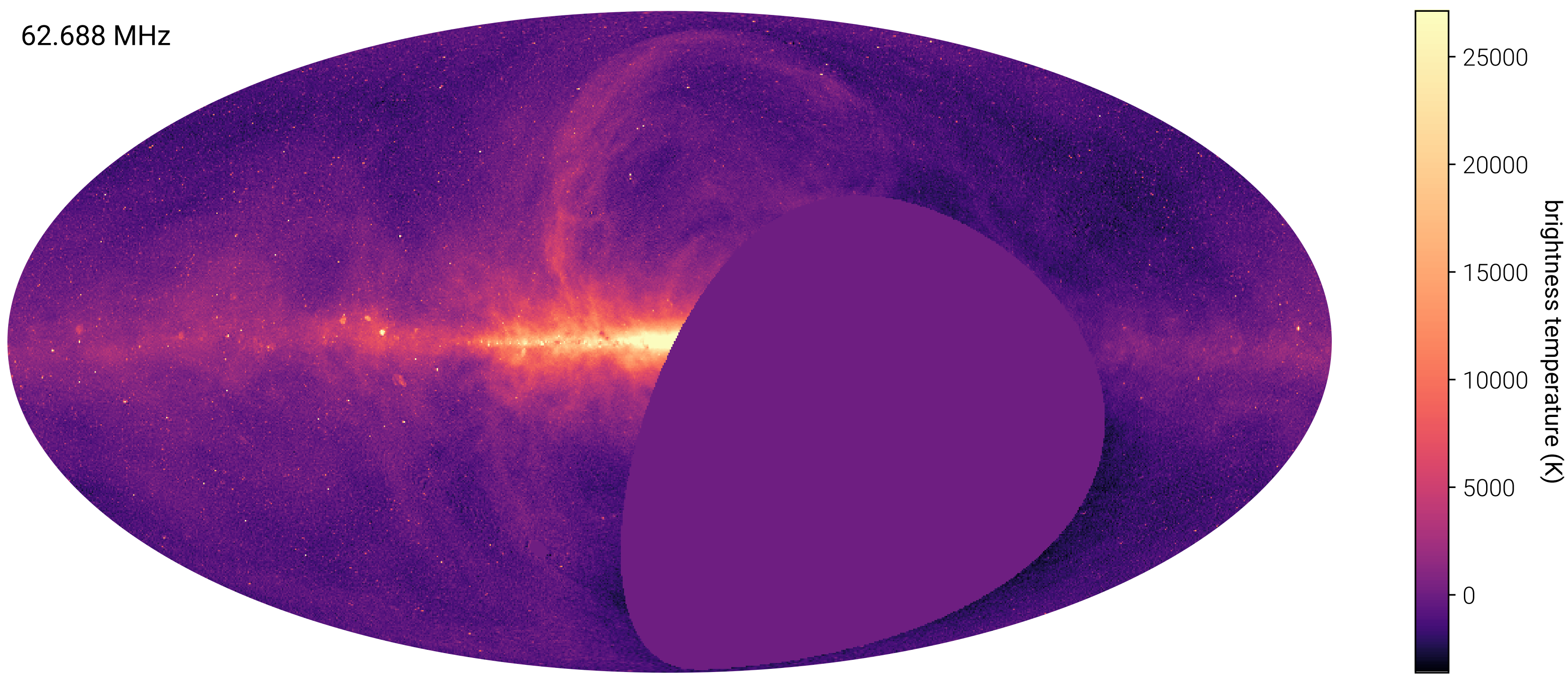

Figure 3.8: continued

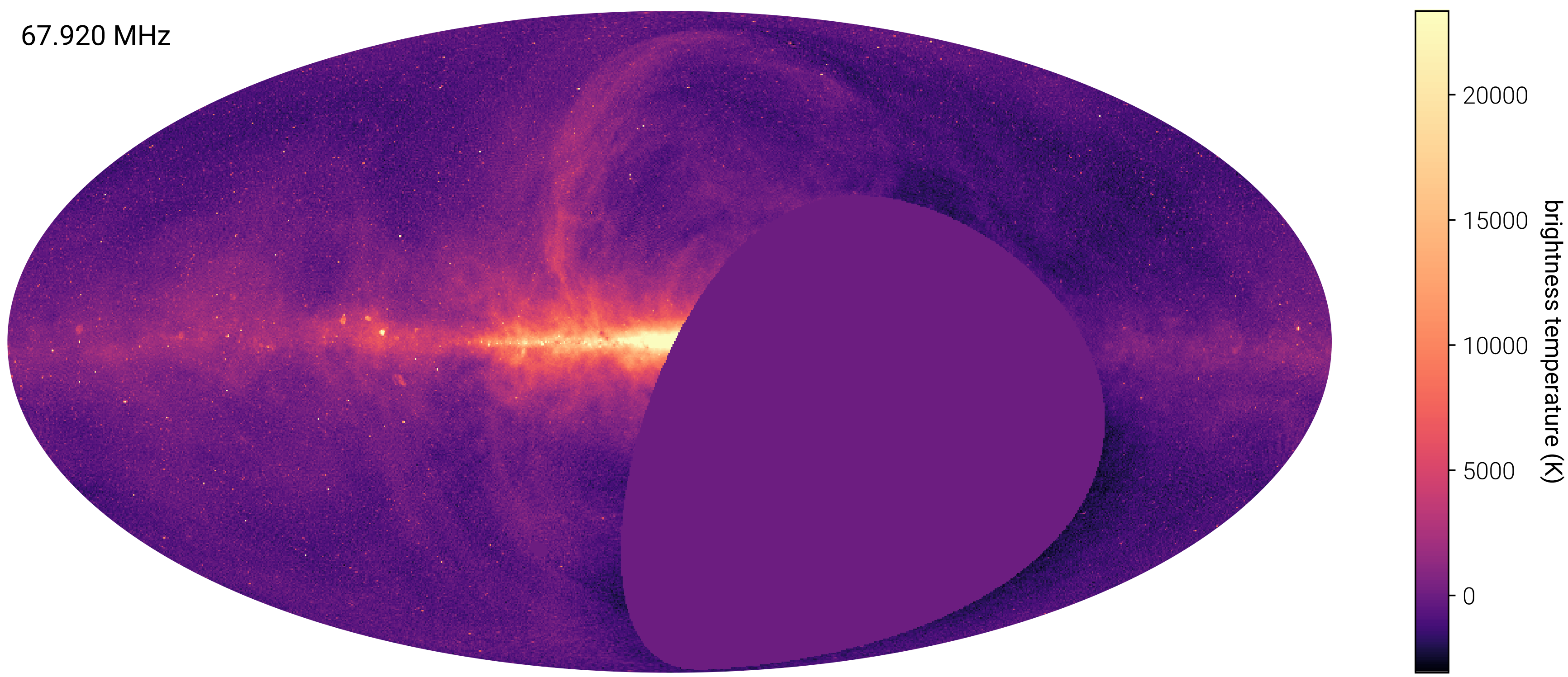

Figure 3.8: continued

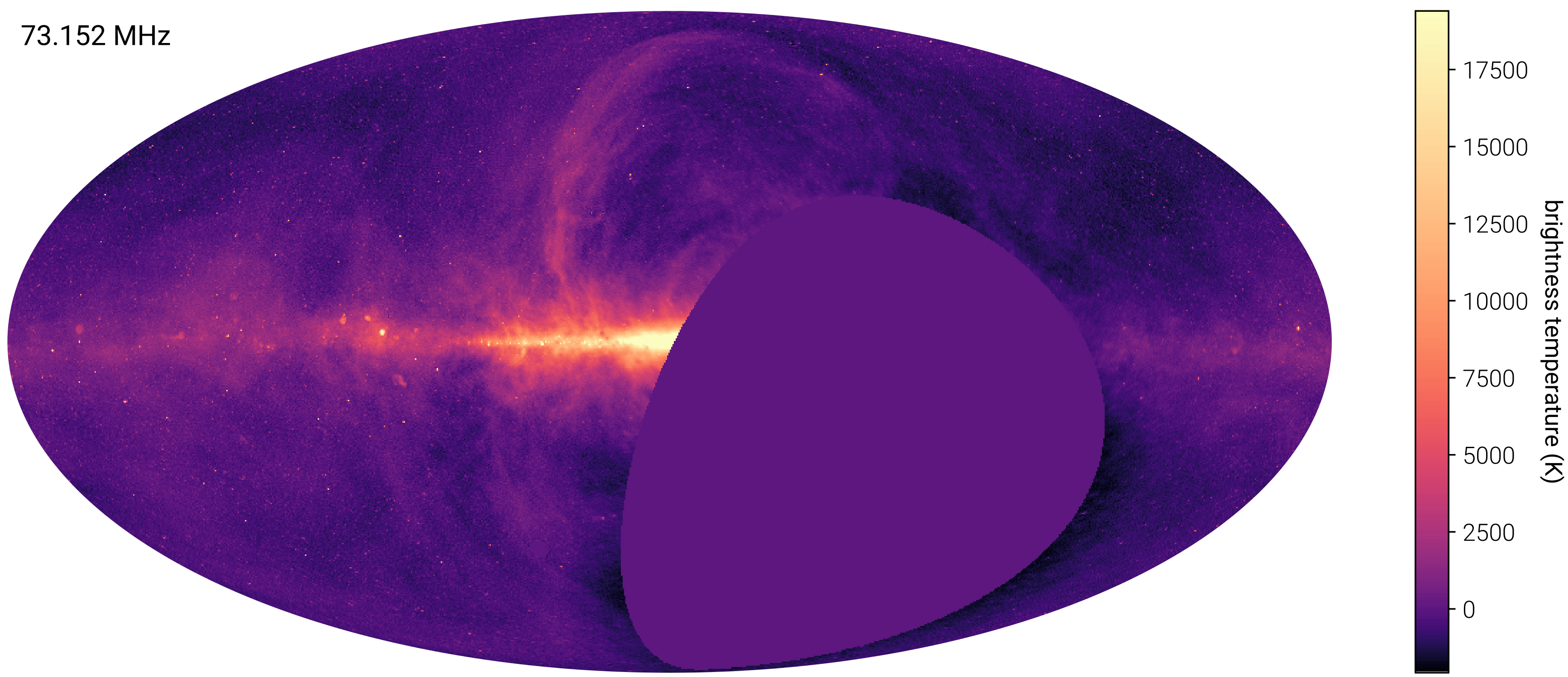

Figure 3.8: continued

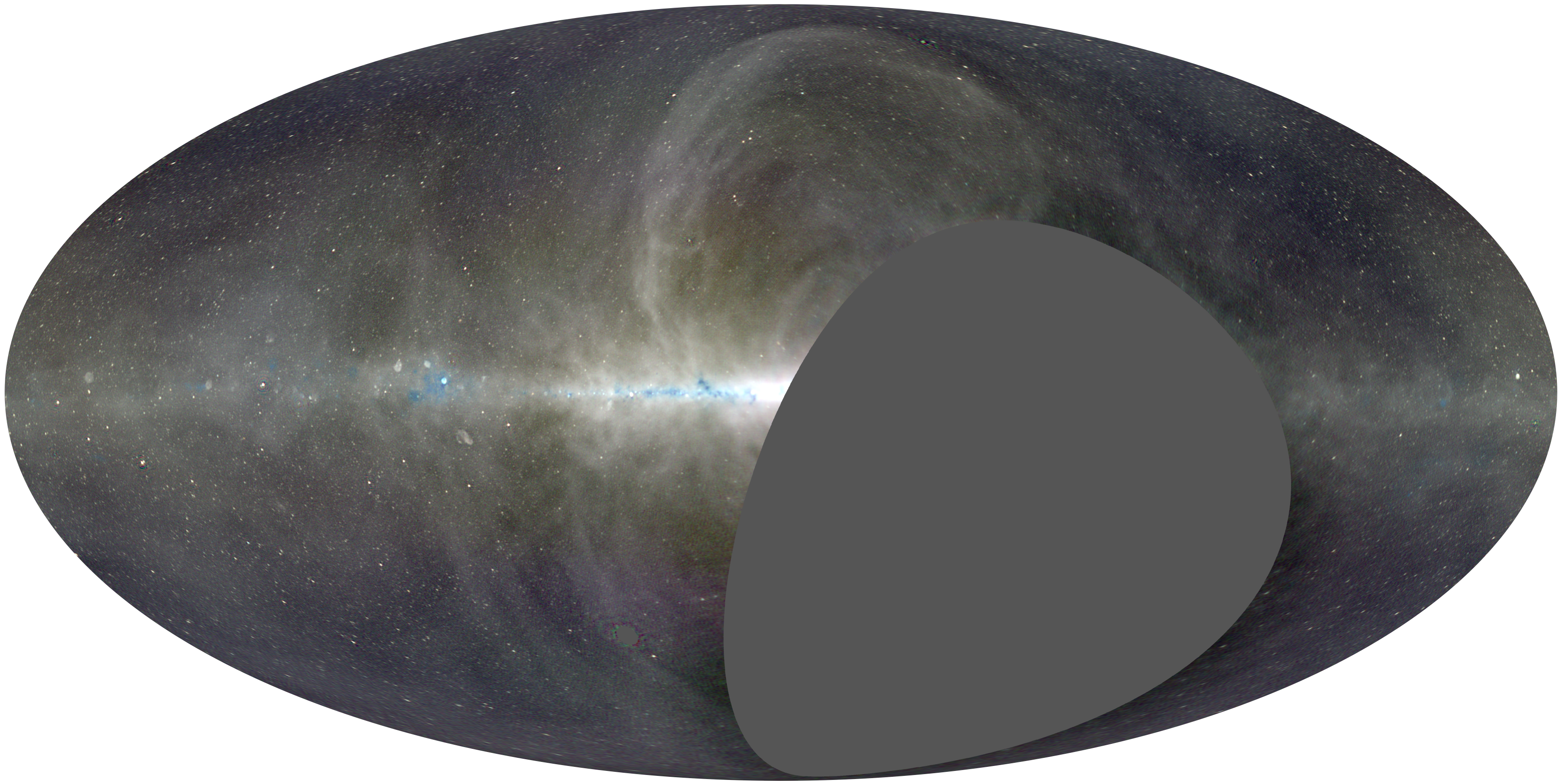

Figure 3.9: This Mollweide-projected map is constructed from three maps of the sky at 36.528 MHz (red), 52.224 MHz (green), and 73.152 MHz (blue). The maps are scaled by $\nu^{2.5}$ before combining, and the color scale is logarithmic (as in Figure 3.8). Therefore, regions with a spectral index of -2.5 will tend to appear white, and regions with a flatter spectral index will tend to appear blue.

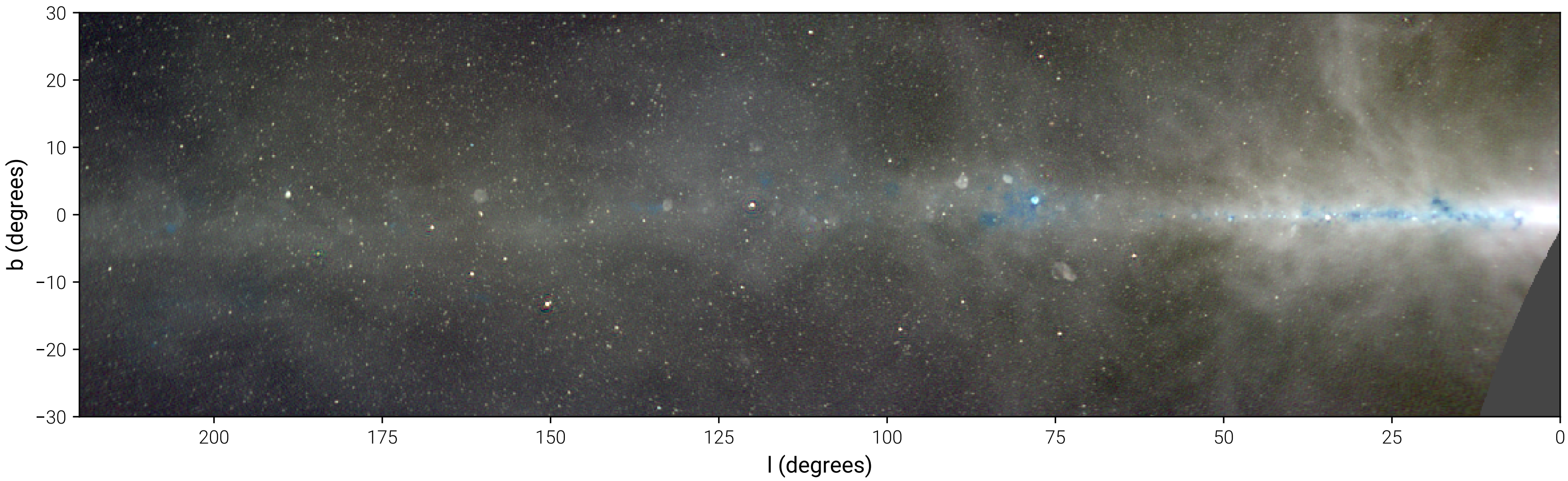

Figure 3.10: Cutout of the galactic plane from Figure 3.9.

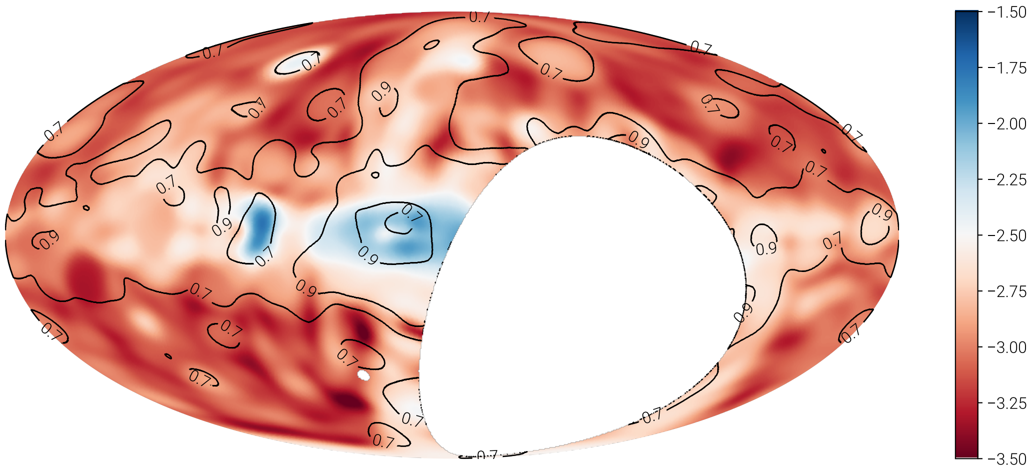

Figure 3.11: Local spectral index measured between the 36.528 MHz map and the 73.152 MHz map estimated by means of a local T–T plot. The color scale gives the spectral index, where blue is flat spectrum and red is steep spectrum. The contours give the coefficient of determination (R^2) for the linear fit to the local T–T plot. If R^2 is low, the quality of the fit is low, and the estimated spectral index is unreliable. This can be due to either insufficient dynamic range in the local T–T plot or multiple emission mechanisms operating in close proximity. Consequently, R^2 tends to drop at higher galactic latitudes (due to dynamic range) and near H II regions in the galactic plane (due to multiple emission mechanisms).

of bright point sources. These rings are naturally removed from the map during CLEANing as long as this filtering step is included in the PSF calculation.

The noise in each map is empirically measured using jackknife resampling. The data set is first split into even- and odd-numbered integrations. These two groups are then imaged and CLEANed independently before being compared against the maps constructed from all of the available data using the jackknife standard error estimator. This estimate of the standard error includes all sources of error that operate on $\sim$ 13 s timescales (the integration time), such as thermal noise and rapid ionospheric fluctuations, but does not account for more slowly varying effects (for example, sidereal variation in the system temperature or day–night fluctuations in the ionosphere). These noise calculations are summarized in Table 3.1. VLSSr source counts (Lane et al., 2014) suggest that the confusion limit at 74 MHz and 15′angular resolution is $\sim 1000 \times (\nu/74\,\mathrm{M}Hz)^{-0.7}$ mJy. Each channel map achieves thermal noise $<$ 900 mJy; therefore, each map is likely at or near the confusion limit.

In the absence of a zero-level correction, a pixel-by-pixel power-law fit to the new

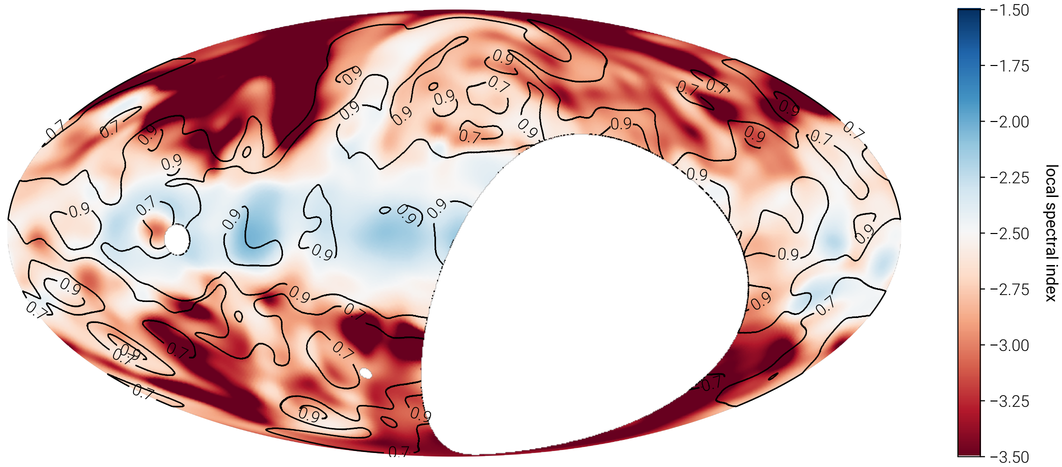

Figure 3.12: Local spectral index measured between the 73.152 MHz OVRO-LWA map and the reprocessed 408 MHz Haslam map (Remazeilles et al., 2015). The color scale gives the spectral index, where blue is flat spectrum and red is steep spectrum. The contours give the coefficient of determination (R^2) for the linear fit to the local T–T plot. See the caption of Figure 3.11 for more details about the coefficient of determination.

maps is impossible. In general, this zero-level correction requires calibrated total power measurements that will be included in future work. Instead, temperature–temperature plots (T–T plots) can be used to measure the spectral index independently of any zero-level corrections (Turtle et al., 1962). This method relies on the assumption that all pixels in a given region are described by the same power law. In that case, there exists a linear relationship between the brightness temperature at frequency ν_1 and frequency ν_2. The slope of this best-fit line is a measure of the spectral index between the two frequencies. The T–T plot can fail to obtain a reliable measure of the spectral index in two ways. First, if there is not enough dynamic range in the emission region, there may be only a weak correlation between the brightness temperature at ν_1 and ν_2. Second, if two emission mechanisms operate in close proximity (i.e., synchrotron and free-free), then a single power-law interpretation of the emission in that region will be poor. Consequently, spectral indices estimated from T–T plots can require careful interpretation.

In Figure 3.11, the spectral index is locally estimated in each part of the sky within a region $\sim 10°$ across by constructing local T–T plots between 36.528 and 73.152 MHz. Contours of constant R^2 (the coefficient of determination) are overlaid. If $R^2 \sim 1$, the spectral index is reliable because there is locally a strong linear correlation between 36.528 and 73.152 MHz. However, if $R^2 \ll 1$, the spectral index calculation is unreliable. R^2 tends to drop in cold patches of the sky where there is not enough dynamic range to find a strong correlation between the two frequencies. It also ends to drop in the vicinity of H II regions in the galactic plane due to multiple emission mechanisms violating the assumption of a single spectral index. Therefore, we should restrict our interpretation of Figure 3.11 to the galactic plane and north galactic spur. In the galactic plane, the synchrotron spectral index varies between ~ -2.5 and -2.75. In the vicinity of H II regions, the spectral index flattens significantly. These H II regions can be seen with higher resolution in Figure 3.10. In Figure 3.10, H II regions appear as blue shadows along the galactic plane due to the increasing impact of free-free absorption at lower frequencies.

In the literature, the spectral index at low frequencies is commonly computed with respect to the Haslam 408 MHz map (Haslam et al., 1981, 1982), which was reprocessed by Remazeilles et al. (2015) to remove artifacts associated with $1/f$ noise and bright sources. Figure 3.12 displays the spectral index computed between the 73.152 MHz map and the reprocessed Haslam map. The spectral index was estimated by degrading the 73.152 MHz map to the resolution of the Haslam map and constructing local T–T plots in every direction. The coefficient of determination is overlaid as a contour plot; however, because $\log(408\,\text{MHz}/73.152\,\text{MHz}) > \log(73.152\,\text{MHz}/36.528\,\text{MHz})$, the spectral indices presented in Figure 3.12 tend to be more robust than those presented in Figure 3.11. This is reflected by the fact that R^2 is larger, but the interpretation must still generally be restricted to the galactic plane.

Comparisons with Other Sky Maps

LWA1 Low Frequency Sky Survey

The LWA1 Low Frequency Sky Survey (LLFSS; Dowell et al., 2017) produced nine maps of the sky between 35 and 80 MHz. Six of these maps are interior to the frequency range spanned by this work. Initial comparisons with the LLFSS helped characterize a systematic rotation in the LWA1's antenna positions. After phase calibration, this manifested itself as a systematic rotation and translation in the snapshot images that were mosaicked to form the final sky map. This systematic error has been corrected in the comparisons presented here and in the latest version of the LLFSS.[7]

[7] Available for download at `http://lda10g.alliance.unm.edu/LWA1LowFrequencySkySurvey/`

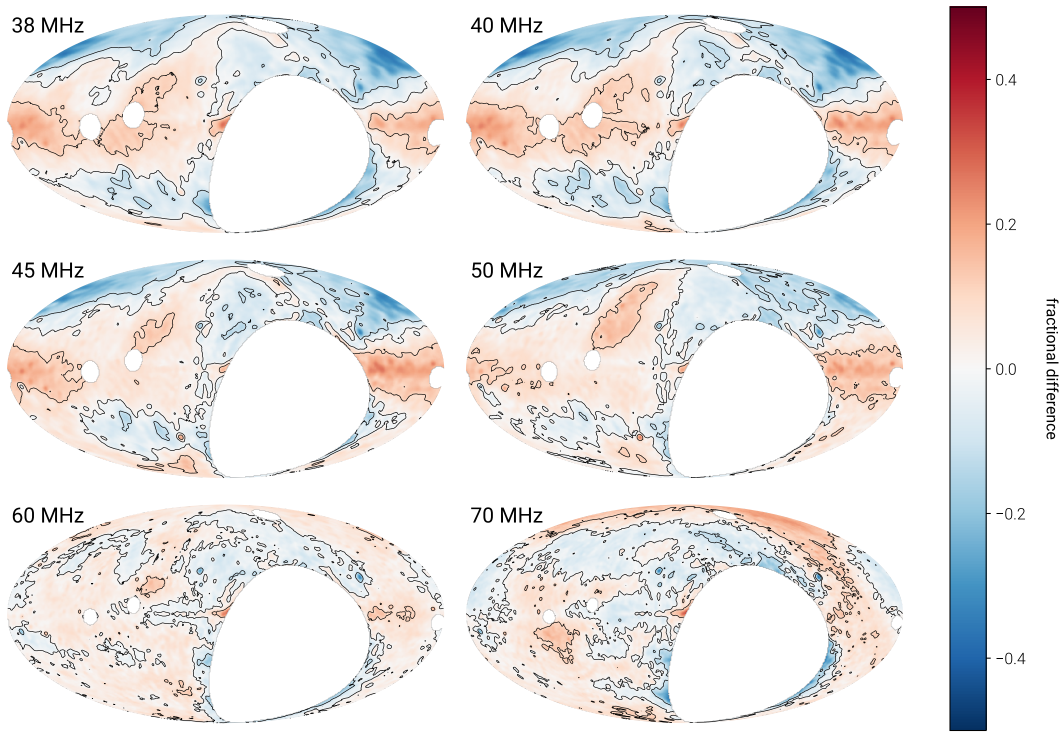

Figure 3.13: Fractional difference between maps from the LLFSS and the OVRO-LWA maps (Figure 3.8) after interpolating to the corresponding frequency and smoothing to the corresponding resolution. A positive value indicates regions where the OVRO-LWA map has more emission that the corresponding LLFSS map. Cas A, Cyg A, Vir A, and Tau A are masked due to the fact that they are subtracted from the OVRO-LWA maps.

A direct comparison with these updated LLFSS maps can be seen in Figure 3.13. In this figure, the LLFSS maps are filtered to remove the monopole and all modes with $m = 0$. The OVRO-LWA maps are interpolated in frequency and blurred to match the angular resolution of the corresponding LLFSS map. At 60 MHz, the agreement is generally better than 10%. However, at lower frequencies the agreement deteriorates to about 20%. Typically, the OVRO-LWA maps have excess emission in the galactic plane and a deficit of emission off the galactic plane relative to the LLFSS.

The LLFSS incorporates calibrated total power radiometry to estimate the missing flux from short spacings. As a result, Dowell et al. (2017) reported per-pixel spectral indices from combining all nine sky maps. Care must be taken in comparing these spectral indices with Figure 3.11 because they are susceptible to different systematic errors. Both calculations are sensitive to mistakes in the antenna primary beam,

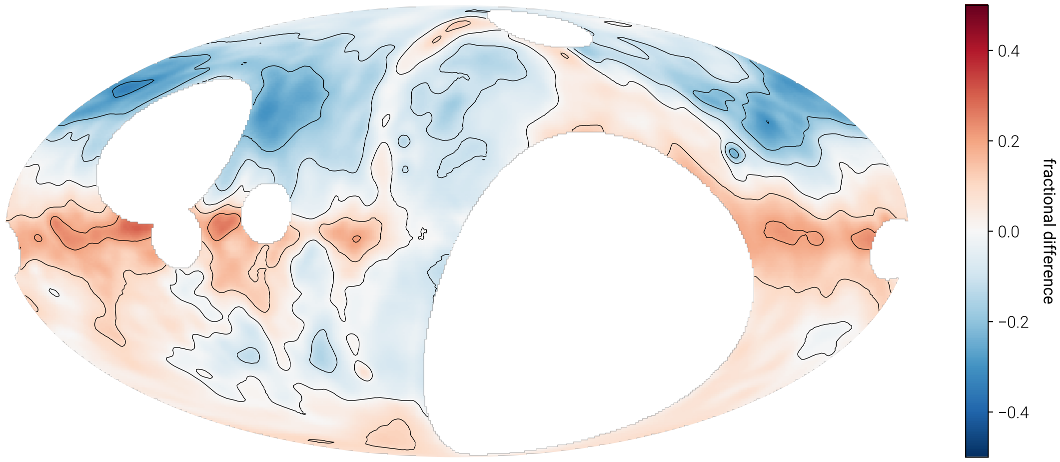

Figure 3.14: This Mollweide-projected map compares the fractional difference between the Guzmán 45 MHz map and the OVRO-LWA maps (Figure 3.8) interpolated to 45 MHz (degraded to 5° resolution). A positive value indicates regions where the OVRO-LWA map has more emission than the Guzmán map, and a negative value indicates regions where the Guzmán map has more emission than the OVRO-LWA map. Cas A, Cyg A, Vir A, and Tau A are masked due to the fact that they are subtracted from the OVRO-LWA maps but not the Guzmán map.

but the LLFSS spectral indices are additionally sensitive to errors in the zero level. We will restrict the comparison to the galactic plane where the spectral indices are likely to be the most reliable. Toward the galactic center, both surveys agree that the spectral index is very flat (> -2.2) due to the influence of free-free absorption. However, at galactic latitudes $\sim 180°$ this work suggests that the spectral index varies between -2.5 and -2.75, while the LLFSS reports substantially flatter indices in the range -2.3 to -2.2. In this region, $0.7 < R^2 < 0.9$ for the OVRO-LWA, so this could be an artifact of the comparatively weak correlation between the brightness at 36.528 and 73.152 MHz, which tends to bias the spectral index toward $-\infty$.

The LLFSS also computes spectral indices with respect to the Haslam 408 MHz map. These spectral indices are subject to the same caveats and systematic errors as before. However, in general, the qualitative agreement with Figure 3.12 is better, potentially due to the increased robustness associated with estimating spectral indices with a larger fractional bandwidth.

Guzmán 45 MHz Map

The Guzmán 45 MHz map (Guzmán et al., 2011) is compiled from a southern hemisphere survey (Alvarez et al., 1997) and a northern hemisphere survey (Maeda et al., 1999), with a small gap around the NCP. In this work, the zero level is set by comparing against published low-frequency measurements in six different directions.

A direct comparison between the OVRO-LWA maps interpolated to 45 MHz and the Guzmán 45 MHz map can be seen in Figure 3.14. In order to make this comparison, the OVRO-LWA map was degraded to a 5° resolution by convolving with a Gaussian kernel, and the Guzmán map has had spherical harmonics with $m = 0$ discarded in order to make it consistent with the maps presented in this paper. This figure shows an $\sim 20\%$ excess of emission in the galactic plane that is consistent with the discrepancy observed between the LLFSS and the Guzmán map. However, while the LLFSS has an excess of emission near the north galactic pole, no such excess is observed in this work. Instead, there is a 10% excess of emission near the south galactic pole. Elsewhere off the plane of the galaxy, the discrepancy can be as much as -20%.

Guzmán et al. (2011) computed the spectral index between their 45 MHz map and the 408 MHz Haslam map. Along the galactic plane, the spectral index varies between -2.2 (in the vicinity of H II regions) and -2.5 (at galactic longitudes $\sim 180°$). The north galactic spur has a spectral index of -2.5. This is generally consistent with the results presented in Figure 3.12.

3.5 Error Analysis

The Ionosphere

One of the key assumptions made by m-mode analysis is that the sky is static. We assume that the only time-dependent behavior is the rotation of the Earth, which slowly rotates the sky through the fringe pattern of the interferometer. At low frequencies, the ionosphere violates this assumption. In particular, ionospheric scintillation and refractive offsets will cause even static sources to exhibit significant variability (Figure 3.5).

The correlation observed on a given baseline for a single point source is

$$V_\nu(t_{\text{sidereal}}) = I_\nu B_\nu(t_{\text{sidereal}}), \tag{3.19}$$

where I_ν is the flux of the source at the frequency ν, and B_ν is the baseline transfer function defined by Equation 3.3. The transfer function is a function of the direction to the source, which is in turn a function of the sidereal time t_{sidereal}. If the source is varying, from intrinsic variability or due to scintillation, then the source flux is also

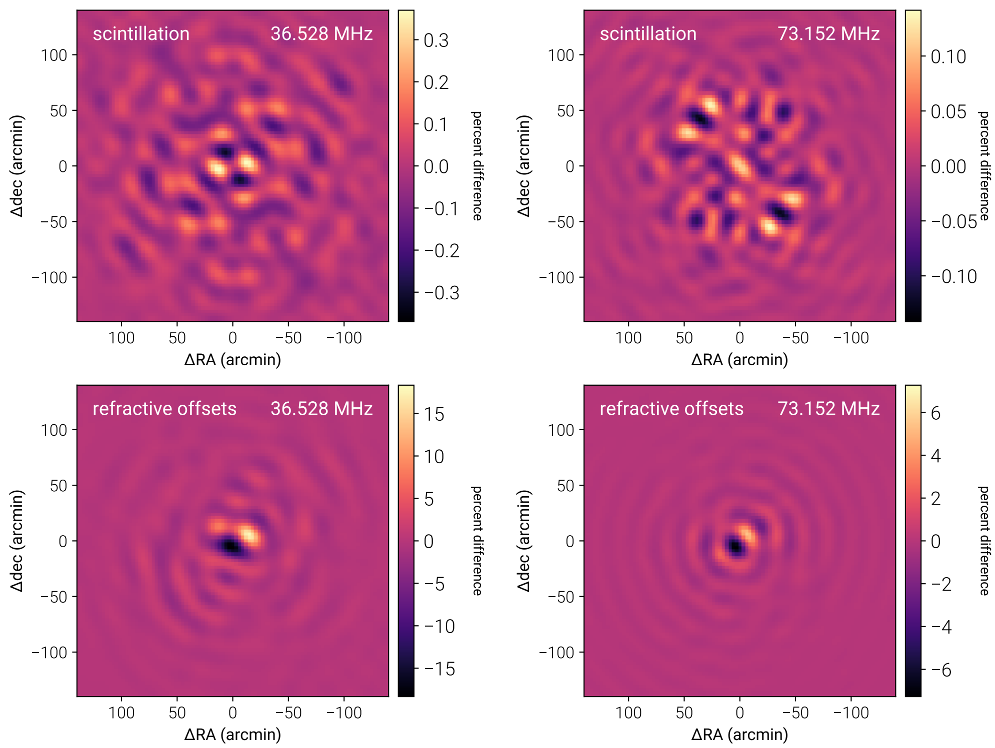

Figure 3.15: Illustration of the corrupting influence of the ionosphere at 36.528 MHz (left column) compared with 73.152 MHz (right column). Each panel shows the simulated PSF for a source at the location of Cas A and illustrates the percent difference (relative to the peak flux of the uncorrupted PSF) due to including an ionospheric effect. In the top row, the simulated source scintillates using the measured light curve for Cas A in Figure 3.5. In the bottom row, the simulated source is refracted from its true position using the measured refractive offsets for Cas A in Figure 3.5.

a function of the time coordinate t such that

$$V_\nu(t_{\text{sidereal}}) = I_\nu(t) B_\nu(t_{\text{sidereal}}), \tag{3.20}$$

where $t_{\text{sidereal}} = (t \mod 23^h 56^m)$.

In order to compute the m-modes, we must take the Fourier transform with respect to the sidereal time. As a consequence of the Fourier convolution theorem, we find

$$V_{\nu,m} \sim \sum_{m'} V_{m'}^{\text{static}} I_{\nu,m-m'}\,, \tag{3.21}$$

where $V_{\nu,m}^{\text{static}}$ is the set of observed m-modes if the source was actually static, and $I_{\nu,m-m'}$ is the Fourier transform of the light curve $I_\nu(t)$. Equation 3.21 indicates that power is scattered between different values of m. As a consequence, the true transfer

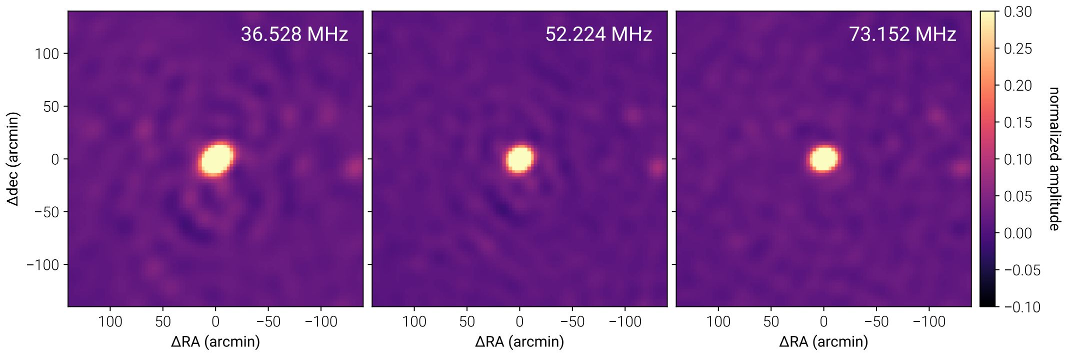

Figure 3.16: Zoom-in of 3C 134 at 36.528 MHz (left panel), 52.224 MHz (middle panel), and 73.152 MHz (right panel). At 36.528 MHz there are $\sim 10\%$ artifacts around 3C 134 that persist after CLEANing due to ionospheric effects. As expected for an ionospheric origin, these artifacts decrease in amplitude as frequency increases. Figure 3.15 shows the typically expected amplitude of these effects for ionospheric scintillation and refractive offsets.

matrix, which is exactly block diagonal in the ideal case, is no longer truly block diagonal (Shaw, 2016).

The maps presented in Figure 3.8 do not account for any off-diagonal terms arising from ionospheric fluctuations. The effect of this can be seen in Figure 3.15. In this simulation, a point source is placed at the location of Cas A. In one case, the source is allowed to scintillate in the same way Cas A does in Figure 3.5, but the source is always located exactly at the location of Cas A. In the second case, the source position is allowed to vary in the same way Cas A does in Figure 3.5, but the flux of the source exactly traces the beam model. The scintillation, although large, introduces only $< 0.3\%$ errors in the vicinity of bright point sources. Refractive offsets, however, can introduce $\sim 15\%$ errors at 36.528 MHz and $\sim 5\%$ errors at 73.152 MHz. Because the sidelobes of the PSF are altered from that of the ideal PSF, refractive offsets will restrict the dynamic range it is possible to obtain with the CLEAN algorithm described in §3.2. This effect can be clearly seen in Figure 3.16, where 10% errors within 1° of 3C 134 are seen at 36.528 MHz. As expected for an ionospheric effect, these errors decrease to a few percent at 52.224 MHz, and less at 73.152 MHz. We therefore conclude that ionospheric effects directly limit the dynamic range in the vicinity of bright point sources.

Beam Errors

A model of the antenna beam is essential for wide-field imaging. Because m-mode analysis imaging operates on a full sidereal day of data, images are constructed after watching each point in the sky move through a large slice of the beam (excepting the celestial poles). The beam model therefore serves two purposes:

1. setting the flux scale as a function of declination and
2. reconciling observations from two separate sidereal times.

In the first case, all sources at a given declination take the same path through the antenna primary beam. If the antenna response is overestimated along this track, then all sources at this declination will have underestimated fluxes. Similarly, if the antenna response is underestimated, then all the sources will have overestimated fluxes. The errors in Figure 3.7 do not show a clear pattern with declination. Two sources have a clear systematic offset at all frequencies: 3C 353 and 3C 380. Source 3C 353 is the second southernmost source, but Hya A – the first southernmost source – does not exhibit this systematic error. Similarly, 3C 380 is at a comparable declination to Lyn A, which appears, if anything, to have its flux systematically offset in the other direction. The absence of a coherent pattern does not eliminate the possibility of beam errors affecting the flux scale, but it does mean that these errors are at least comparable to the errors inherent to the flux scale itself.

The second case is more subtle. Sources are observed at a wide range of locations in the primary beam of the antenna. The imaging process must reconcile all of these observations together, and the beam model provides the instructions for how to do this. In the event of an error in the beam model, it can be expected that the beam will introduce errors into the sky maps that will limit the dynamic range in the vicinity of bright point sources. Shaw et al. (2015) simulated the effect of beam errors on a cosmological analysis, concluding that the beam must be known to one part in 10^4. Our requirements are significantly less stringent because we are estimating the sky brightness instead of estimating the amplitude of a faint cosmological signal in the presence of foreground emission that dominates the signal by five orders of magnitude. In fact, in §3.5 we found that ionospheric effects likely dominate over other sources of error that affect the PSF shape. Therefore, we conclude that the beam models generated in §3.3 are sufficient to limit the effect of beam errors on the PSF to at least less than those introduced by the ionosphere.

Polarization Leakage

Shaw et al. (2015) described how to generalize m-mode analysis to account for a polarized sky observed with a polarized antenna beam. Heretofore, this generalization has been neglected in the discussion of m-mode analysis imaging. At low frequencies, increasingly rapid Faraday rotation leads to depolarization. Therefore, polarization fractions are generally expected to decrease at low frequencies (varying with ionospheric conditions). Lenc et al. (2016) detected the presence of diffuse polarized emission on degree angular scales with the MWA, also finding typical depolarization ratios of ~ 0.3 for pulsars at 154 MHz relative to 1.4 GHz, although there was a large variance between pulsars. Even more depolarization is expected at frequencies $\leq$ 73.152 MHz, but crossed-dipole antennas with extremely large primary beams will naturally introduce large polarization leakage terms at low elevations. It is instructive to compute what impact this will have on the unpolarized imaging process.

In order to understand the effect of polarization leakage, we simulated a point source with 10% polarization in Stokes Q at the location of Cas A. The simulated visibilities were computed using the measured beams for the x and y dipoles. Because the amplitudes of the two beams are not equal in every direction on the sky, this introduces a direction-dependent leakage of Stokes Q into Stokes I. At 73.152 MHz, this leakage is $\lesssim 5\%$ above 15° elevation but rapidly rises to $\gtrsim 50\%$ at lower elevations. Obenberger et al. (2015) reported similar polarization leakage measurements with the LWA1. Cas A is a circumpolar source and spends about 7 hours every day skirting the horizon where the polarization leakage is large, so by placing the simulated source at the location of Cas A, we are engineering a situation where the polarization leakage from Stokes Q into Stokes I will be large. However, the impact on the unpolarized m-mode analysis maps is mild, amounting to a 0.5% error in the flux of the source.

Terrestrial Interference and Pickup

When writing Equation 3.2, it is implicitly assumed that the correlated voltage fluctuations measured between pairs of antennas are exclusively generated by astronomical sources of radio emission. In practice, this assumption can be violated. For instance, a low-frequency interferometer located in the vicinity of an arcing power line will see an additional contribution from the RFI generated by the arcing process. Similarly, common-mode pickup along the analog signal path of the interferometer may generate an additional spurious contribution to the measured visibilities. While the amplitude and phase of these contaminating signals may fluctuate with time, they do not sweep across the sky at the sidereal rate characteristic of astronomical sources.

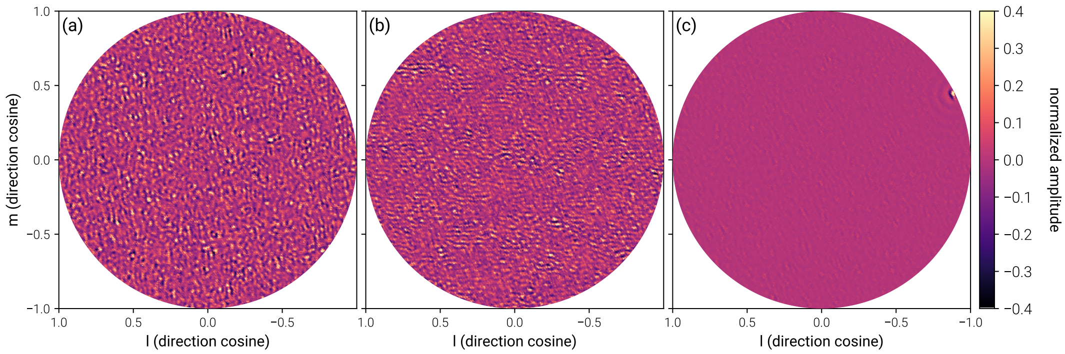

Figure 3.17: Terrestrial sources of correlated noise that are apparent after averaging the visibilities at 62.688 MHz over the entire 28 hour observing period (keeping the phase center at zenith such that astronomical sources of radio emission are smeared along tracks of constant declination). Each panel represents a different component that is removed from the visibilities. The images are generated using WSClean (Offringa et al., 2014), uniform weighting, and only baselines longer than 15 wavelengths. Panels (a) and (b) illustrate components that appear noise-like in image space, but are in fact a constant offset to the measured visibilities likely associated with cross-talk or common-mode pickup. Panel (c) illustrates a component that is clearly associated with an RFI source on the horizon to the west–northwest of the OVRO-LWA. This RFI source is likely an arcing power line. Figure 3.18 illustrates the characteristic ringlike artifacts introduced into the maps if these three components are not removed prior to m-mode analysis imaging. The component shown in panel (a) has about twice the amplitude ($\|\boldsymbol{v}_{\text{terrestrial}}\|$) of those in panels (b) and (c), and for all three components, $\|\boldsymbol{B}^*\boldsymbol{v}_{\text{terrestrial}}\|/(\|\boldsymbol{B}\|\|\boldsymbol{v}_{\text{terrestrial}}\|) \sim 0.035$.

The Owens Valley is an important source of water and power for the city of Los Angeles. Unfortunately, this means that high-voltage power lines run along the valley $\gtrsim$ 10 km to the west of the OVRO-LWA. Some of these power-line poles have faulty insulators that arc and produce pulsed, broadband RFI. Because these poles exist in the near-field of the array, we have been able to localize some of them by using the curvature of the incoming wavefront to infer a distance. Efforts are currently underway to work with the utility pole owners to have these insulators replaced.

In the meantime, it is possible to suppress their contamination in the data set. The contribution of these RFI sources to the visibilities can be plainly seen by averaging > 24 hours of data with the phase center set to zenith. In this way, true sky components are smeared along tracks of constant declination while terrestrial sources (i.e., the arcing power lines or any contribution due to common-mode pickup) are not smeared. Obtaining a model for the RFI is complicated by the fact that the

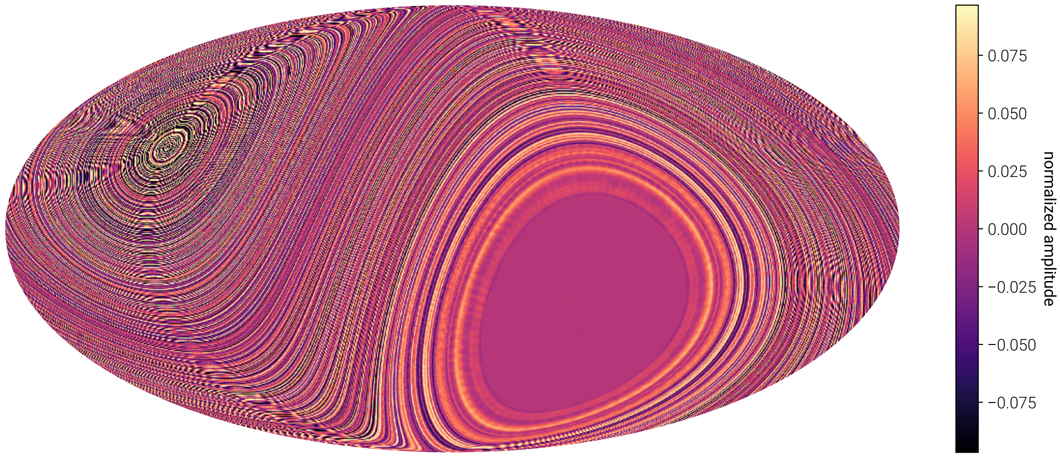

Figure 3.18: A Mollweide-projected image of the artifacts introduced to the m-mode analysis maps by the three terrestrial sources shown in Figure 3.17. Because these sources are not moving through the sky sidereally, they tend to be smeared along rings of constant declination. The spurs seemingly radiating from the NCP are a Moiré pattern (i.e., an artifact of the pixelization).

contaminating sources are at extremely low elevations, where the antenna response is essentially unknown (and inhomogeneous due to antenna shadowing effects). It is not enough to know the physical location of the faulty insulator generating the RFI. In addition, we must know the response of each antenna (amplitude and phase) in the appropriate direction. This motivates the use of peeling, which allows the antenna response to be a free parameter. Therefore, model visibilities for the RFI can be obtained by peeling the sources after smearing the visibilities over > 24 hours. Figure 3.17 shows an illustration of some of the removed components at 62.688 MHz.

While attempting to peel RFI sources from the averaged visibilities, it was discovered that frequently peeling would remove components from the visibilities that are not obviously associated with any source on the horizon or elsewhere in the sky (see panels (a) and (b) in Figure 3.17). These components appear noise-like in the images, but they are actually a constant offset to the measured visibilities and are therefore likely associated with cross-talk or some form of common-mode pickup. If these components are not subtracted from the measured visibilities, they contribute ringlike structures to the sky maps, as seen in Figure 3.18. This figure is not a simulation but rather a difference between maps created before and after measuring and subtracting the components in Figure 3.17 from each integration.

The first step in Equation 3.9 is to compute $\boldsymbol{B}^*\boldsymbol{v}$. In this step, we compute the projection of the measurement $\boldsymbol{v}$ onto the space spanned by the columns of $\boldsymbol{B}$. Each column of $\boldsymbol{B}$ describes the interferometer's response to a corresponding spherical harmonic coefficient of the sky-brightness distribution. Therefore, the act of computing $\boldsymbol{B}^*\boldsymbol{v}$ is to project the measured m-modes onto the space of m-modes that could be generated by astronomical sources. The degree to which a source of terrestrial interference will contaminate a map generated using m-mode analysis imaging is determined by its amplitude after projection.

For instance, a bright interfering source might contribute $\boldsymbol{v}_{\text{terrestrial}}$ to the measured m-modes. However, if $\boldsymbol{v}_{\text{terrestrial}}$ is actually perpendicular to all of the columns of $\boldsymbol{B}$, there will be no contamination in the map because $\boldsymbol{B}^*\boldsymbol{v}_{\text{terrestrial}} = \boldsymbol{0}$. In practice, this is unlikely. In general, the contamination is proportional to the overall amplitude of the interference ($\|\boldsymbol{v}_{\text{terrestrial}}\|$) and the degree to which the interference mimics an astronomical signal ($\|\boldsymbol{B}^*\boldsymbol{v}_{\text{terrestrial}}\|/(\|\boldsymbol{B}\|\|\boldsymbol{v}_{\text{terrestrial}}\|)$).

These terrestrial sources do not rotate with the sky, and hence their contamination tends to be restricted to modes with small m. In this data set the contamination is largely restricted to $m \lesssim 1$. Although the RFI is capable of fluctuating on short timescales, in this case, the artifacts it introduces seem to be restricted to small m (presumably because the phase is not fluctuating). As a result, if the contamination is not suppressed, it will manifest itself as rings along stripes of constant declination. This effect is plainly visible in Figure 3.17. Because of the distinctive ringlike pattern created by terrestrial sources, we additionally chose to discard spherical harmonics with either $m = 0$ or $m = 1$ and $l > 100$ in order to further suppress the contamination.

3.6 Conclusion

In this work, we presented a new imaging technique – Tikhonov-regularized m-mode analysis imaging and CLEANing – for drift-scanning telescopes like the OVRO-LWA. This technique exactly corrects for wide-field effects in interferometric imaging with a single synthesis imaging step. We applied Tikhonov-regularized m-mode analysis imaging to a 28 hour data set and generated eight sky maps between 36.528 and 73.152 MHz. These sky maps are a substantial improvement in angular resolution over existing maps at these frequencies with $\sim 15'$ angular resolution and < 600 K thermal noise. The point-source flux scale is consistent with that defined by Scaife & Heald (2012) to about 5%, and large angular scales are consistent with the work of Dowell et al. (2017) to within 20%.

At frequencies above ∼ 55 MHz, the angular resolution of these maps is limited by the selection of $l_{max} = 1000$. Future work will increase l_{max} to remove this restriction, as well as include more time and bandwidth to improve the thermal noise. The usage of nighttime-only data can help mitigate dynamic range limitations from the ionosphere and also eliminate solar sidelobe residuals. Observations could also be extended to slightly higher and lower frequencies (∼ 27 to 85 MHz) to take advantage of the full frequency range of the OVRO-LWA. The higher frequencies are particularly interesting in order to maximize the overlap with the MWA in the southern hemisphere, which could be used to fill in the hole around the southern celestial pole.

These maps and future improvements are primarily intended to be used as part of a foreground modeling and subtraction routine for 21 cm cosmology experiments. Each map will be made publicly available on LAMBDA.

Acknowledgments

This work is dedicated to the memory of Professor Marjorie Corcoran, who was an influential mentor to MWE.

This material is based in part upon work supported by the National Science Foundation under grants AST-1654815 and AST-1212226. The OVRO-LWA project was initiated through the kind donation of Deborah Castleman and Harold Rosen.

Part of this research was carried out at the Jet Propulsion Laboratory, California Institute of Technology, under a contract with the National Aeronautics and Space Administration, including partial funding through the President's and Director's Fund Program.

This work has benefited from open-source technology shared by the Collaboration for Astronomy Signal Processing and Electronics Research (CASPER). We thank the Xilinx University Program for donations; NVIDIA for proprietary tools, discounts, and donations; and Digicom for collaboration on the manufacture and testing of DSP processors.

We thank the Smithsonian Astrophysical Observatory Submillimeter Receiver Lab for the collaboration of its members.

Development, adaptation, and operation of the LEDA real-time digital signal-processing systems at OVRO-LWA have been supported in part by NSF grants AST/1106059, PHY/0835713, and OIA/1125087.

GBT, JD, and FKS acknowledge support from the National Science Foundation under grant AST-1139974.

Bibliography

Ali, Z. S., Parsons, A. R., Zheng, H., et al. 2015, ApJ, 809, 61

Alvarez, H., Aparici, J., May, J., & Olmos, F. 1997, A&AS, 124, 205

Baars, J. W. M., Genzel, R., Pauliny-Toth, I. I. K., & Witzel, A. 1977, A&A, 61, 99

Beardsley, A. P., Hazelton, B. J., Sullivan, I. S., et al. 2016, ApJ, 833, 102

Berger, P., Oppermann, N., Pen, U.-L., & Shaw, J. R. 2016, ArXiv e-prints, arXiv:1612.03255

Bezanson, J., Edelman, A., Karpinski, S., & Shah, V. B. 2017, SIAM Review, 59, 65. http://dx.doi.org/10.1137/141000671

Bhatnagar, S., Rau, U., & Golap, K. 2013, ApJ, 770, 91

Bowman, J. D., Rogers, A. E. E., Monsalve, R. A., Mozdzen, T. J., & Mahesh, N. 2018, Nature, 555, 67

Briggs, D. S. 1995, phdthesis, The New Mexico Institute of Mining and Technology

Chapman, E., Abdalla, F. B., Bobin, J., et al. 2013, MNRAS, 429, 165

Cornwell, T. J., Golap, K., & Bhatnagar, S. 2008, IEEE Journal of Selected Topics in Signal Processing, 2, 647

de Oliveira-Costa, A., Tegmark, M., Gaensler, B. M., et al. 2008, MNRAS, 388, 247

DeBoer, D. R., Parsons, A. R., Aguirre, J. E., et al. 2016, ArXiv e-prints, arXiv:1606.07473

Dowell, J., Taylor, G. B., Schinzel, F. K., Kassim, N. E., & Stovall, K. 2017, MNRAS, 469, 4537

Ewall-Wice, A., Dillon, J. S., Hewitt, J. N., et al. 2016, MNRAS, 460, 4320

Fialkov, A., Barkana, R., Pinhas, A., & Visbal, E. 2014, MNRAS, 437, L36

Furlanetto, S. R., Oh, S. P., & Briggs, F. H. 2006, Phys. Rep., 433, 181

Greig, B., & Mesinger, A. 2015, MNRAS, 449, 4246

Guzmán, A. E., May, J., Alvarez, H., & Maeda, K. 2011, A&A, 525, A138

Górski, K. M., Hivon, E., Banday, A. J., et al. 2005, ApJ, 622, 759

Hallinan, G., et al. in prep.

Haslam, C. G. T., Klein, U., Salter, C. J., et al. 1981, A&A, 100, 209

Haslam, C. G. T., Salter, C. J., Stoffel, H., & Wilson, W. E. 1982, A&AS, 47, 1

Heald, G. H., Pizzo, R. F., Orrú, E., et al. 2015, A&A, 582, A123

Helmboldt, J. F., & Kassim, N. E. 2009, AJ, 138, 838

Högbom, J. A. 1974, A&AS, 15, 417

Iijima, B. A., Harris, I. L., Ho, C. M., et al. 1999, Journal of Atmospheric and Solar-Terrestrial Physics, 61, 1205

Intema, H. T., Jagannathan, P., Mooley, K. P., & Frail, D. A. 2017, A&A, 598, A78

Johnson, S. G. 2008, The NLopt nonlinear-optimization package, `http://ab-initio.mit.edu/nlopt`, ,

Kassim, N. E., Lazio, T. J. W., Erickson, W. C., et al. 2007, ApJS, 172, 686

Kintner, Jr., P. M., Coster, A. J., Fuller-Rowell, T., et al. 2008, Washington DC American Geophysical Union Geophysical Monograph Series, 181, doi:10.1029/GM181

Kocz, J., Greenhill, L. J., Barsdell, B. R., et al. 2015, Journal of Astronomical Instrumentation, 4, 1550003

Lane, W. M., Cotton, W. D., van Velzen, S., et al. 2014, MNRAS, 440, 327

Lenc, E., Gaensler, B. M., Sun, X. H., et al. 2016, ApJ, 830, 38

Maeda, K., Alvarez, H., Aparici, J., May, J., & Reich, P. 1999, A&AS, 140, 145

Mevius, M., van der Tol, S., Pandey, V. N., et al. 2016, Radio Science, 51, 927

Mitchell, D. A., Greenhill, L. J., Wayth, R. B., et al. 2008, IEEE Journal of Selected Topics in Signal Processing, 2, 707

Monsalve, R. A., Rogers, A. E. E., Bowman, J. D., & Mozdzen, T. J. 2017, ApJ, 847, 64

Mozdzen, T. J., Bowman, J. D., Monsalve, R. A., & Rogers, A. E. E. 2017, MNRAS, 464, 4995

Obenberger, K. S., Taylor, G. B., Hartman, J. M., et al. 2015, Journal of Astronomical Instrumentation, 4, 1550004

Offringa, A. R., McKinley, B., Hurley-Walker, N., et al. 2014, MNRAS, 444, 606

Parsons, A. R., Pober, J. C., Aguirre, J. E., et al. 2012, ApJ, 756, 165

Patil, A. H., Yatawatta, S., Koopmans, L. V. E., et al. 2017, ApJ, 838, 65

Perley, R. A., & Butler, B. J. 2017, ApJS, 230, 7

Pober, J. C., Parsons, A. R., Jacobs, D. C., et al. 2012, AJ, 143, 53

Price, D. C., Greenhill, L. J., Fialkov, A., et al. 2017, ArXiv e-prints, arXiv:1709.09313

Pritchard, J. R., & Loeb, A. 2012, Reports on Progress in Physics, 75, 086901

Refregier, A. 2003, MNRAS, 338, 35

Remazeilles, M., Dickinson, C., Banday, A. J., Bigot-Sazy, M.-A., & Ghosh, T. 2015, MNRAS, 451, 4311

Rowan, T. 1990, phdthesis, Department of Computer Sciences, University of Texas at Austin

Salvini, S., & Wijnholds, S. J. 2014, A&A, 571, A97

Scaife, A. M. M., & Heald, G. H. 2012, MNRAS, 423, L30

Shaw, J. R. 2016, private communication, ,

Shaw, J. R., Sigurdson, K., Pen, U.-L., Stebbins, A., & Sitwell, M. 2014, ApJ, 781, 57

Shaw, J. R., Sigurdson, K., Sitwell, M., Stebbins, A., & Pen, U.-L. 2015, Phys. Rev. D, 91, 083514

Singh, S., Subrahmanyan, R., Udaya Shankar, N., et al. 2017, ArXiv e-prints, arXiv:1703.06647

Smirnov, O. M., & Tasse, C. 2015, MNRAS, 449, 2668

Sokolowski, M., Tremblay, S. E., Wayth, R. B., et al. 2015, PASA, 32, e004

Thompson, A. R., Moran, J. M., & Swenson, Jr., G. W. 2001, Interferometry and Synthesis in Radio Astronomy, 2nd Edition

Turtle, A. J., Pugh, J. F., Kenderdine, S., & Pauliny-Toth, I. I. K. 1962, MNRAS, 124, 297

Vedantham, H. K., & Koopmans, L. V. E. 2015, MNRAS, 453, 925

Venumadhav, T., Chang, T.-C., Doré, O., & Hirata, C. M. 2016, ApJ, 826, 116

Voytek, T. C., Natarajan, A., Jáuregui García, J. M., Peterson, J. B., & López-Cruz, O. 2014, ApJ, 782, L9

Wayth, R. B., Lenc, E., Bell, M. E., et al. 2015, PASA, 32, e025

Zheng, H., Tegmark, M., Dillon, J. S., et al. 2017a, MNRAS, 464, 3486

—. 2017b, MNRAS, 465, 2901

Chapter 4

21 CM COSMOLOGY OF THE COSMIC DAWN: FIRST SPATIAL POWER SPECTRUM LIMITS WITH THE OVRO-LWA

Chapter 5

CONCLUSION

Appendix A

OPEN-SOURCE SOFTWARE

A.1 CasaCore.jl

A.2 LibHealpix.jl

A.3 UnitfulAstro.jl